EXPLORATIONS ON OPTOMECHANICAL DEVICES FOR ENERGY SINK APPLICATIONS

A THESIS SUBMITTED TO

THE GRADUATE SCHOOL OF ENGINEERING AND SCIENCE

OF BILKENT UNIVERSITY

IN PARTIAL FULFILLMENT OF THE REQUIREMENTS FOR

THE DEGREE OF

MASTER OF SCIENCE

IN

MATERIAL SCIENCE AND NANOTECHNOLOGY

By

ChulHyeong Lee

January 2023

Explorations on Optomechanical Devices for Energy Sink Applications
By ChulHyeong Lee
January 2023

We certify that we have read this thesis and that in our opinion it is fully adequate, in scope and in quality, as a thesis for the degree of Master of Science.

Mehmet Selim Hanay(Advisor)

Emine Yegan Erdem

Burhanettin Erdem Alaca

Approved for the Graduate School of Engineering and Science:

Orhan Arıkan
Director of the Graduate School

ABSTRACT

EXPLORATIONS ON OPTOMECHANICAL DEVICES FOR ENERGY SINK APPLICATIONS

ChulHyeong Lee
M.S. in Material Science and Nanotechnology
Advisor: Mehmet Selim Hanay
January 2023

Resonance energy dissipation mechanism has been gaining importance in the interest of sensing applications. As such, the capacity for precise and fast measurement of the transient phase of motion has been desirable. The development of optomechanics in recent years has enabled such a fast scheme.

Here a design, setup, and measurement of a silicon nitride optomechanical system is explored. Fundamental parameters of the design are investigated with simulation analysis. Grating structures, waveguides, and resonator parameters are explored. A series of optical resonance responses are observed, and the resonance characteristics are analyzed for optomechanical devices of combinations of design parameters. Measurements on devices of different nanomechanical beam modulation schemes are performed. To translate the technique from the optical to microwave domain, an integration of a split ring resonator (SRR) cavity and NEMS device is explored. Mode simulation of the modified cavity design is done. A technique of alignment of EBL to an existing pattern on an insulating surface is optimized. The studied designs leave possibilities for applications in real-time mass sensing and fundamental studies on energy dissipation mechanisms.

Keywords: NEMS, Optomechanics, Ring Resonators, Racetrack Resonators, Microwave Cavity.

ÖZET

ENERJİ SÖNÜMLEME UYGULAMALARINDA OPTOMEKANİK AYGITLARIN KULLANIMI

ChulHyeong Lee
Material Science and Nanotechnology, Yüksek Lisans
Tez Danışmanı: Mehmet Selim Hanay
Ocak 2023

Rezonans enerjisi dağılım mekanizması, algılama uygulamaları alanında önem kazanmaktadır. Buna istinaden hareketin geçici halinde, hızlı ve kesin ölçüm kapasitesine ulaşmak hedeflenmektedir. Optomekanik teknolojisindeki son yıllardaki gelişmeler bu şekilde hızlı bir sistemi ulaşılabilir kılmıştır.

Bu çalışmada, bir silisyum nitrür optomekanik sistemin tasarımı, kurulumu ve ölçümü incelenmiştir.

Dizaynın temel parametreleri, simülasyon analizleriyle incelenmiştir. Saçılım ızgaraları, dalga kılavuzları ve rezonatör parametreleri araştırılmış ve değerlendirilmiştir. Bir dizi optik rezonans yanıtları gözlemlenmiş ve, dizayn parametrelerinin farklı kombinasyonlarındaki optomekanik cihazlar için rezonans karakteristikleri incelenmiştir.

Farklı nanomekanik ışın modülasyon düzenlerindeki cihazlarda ölçümler yapılmıştır. Bu tekniği optik alanından mikrodalga alanına çevirmek için bir Bölünmüş halka rezonatörü (SRR) kavitesi ve NEMS cihazı araştırılmıştır. Değiştirilmiş (modified) kavite tasarımın mod simülasyonu yapılmıştır. Yalıtım sağlayıcı bir yüzeyde önceden var olan bir düzene(pattern), Elektron Işın Litografisi (EBL) hizalama tekniği en iyi hale getirilmeye çalışılmıştır.

Çalışılan tasarımlar, gerçek zamanlı kütle ölçümü uygulamalarında ve enerji dağılım mekanizmalarındaki temel araştırmalarda yeni olanak olduğunu göstermektedir.

Anahtar sözcükler: NEMS, Optomekanik, Halka Rezonatörler, Parkur Rezonatörler,Mikrodalga Boşluğu.

Acknowledgement

I extend my gratitude to my advisor Prof. Mehmet Selim Hanay for his guidance and support. Since undergraduate times, he has been one of the key figures to me with intuitive teachings and perspectives, and it has overflown to my masters career. Those are valuable lessons to me that I will treasure.

I thank Dr. Hashim Alhmoud, Sayedus Salehin, Ceren Alataş, Enise Kartal, Mohammed Alkhaled, Batuhan Kaynak, Burak Sarı, and Uzay Tefek. These guys have been of great helps to carry on my work in this group, from helps in fabrications or measurements to some random chats that are refreshing. The discussions about and unrelated to the work are all fond memories of mine. I also thank the former members of Hanay group, Berke Demiralp, Oğuzhan Yücel, Berk Küçükoğlu, Atakan Arı and Dr. Pisheh for giving me a head-start in my fabrication work. I acknowledge Rumon, who was a PhD student I met at UNAM being my EBL buddy. I thank those who helped with the fabrication, Dr Cenk from Sabanci University and Murat and Kadir from Metu MEMS.

I thank all those who motivated me for my love for science. I thank Prof. Seymour Jahangirov for his beautiful insights in science and learning, and extending it to other things in life such as music with great analogies. I have been introduced to Richard Feynman by him, from whom I have vicariously experienced an exquisite way of approaching and understanding things in life scientifically.

I am grateful for Arda Karaşahin, who was my undergraduate colleague who was my senior project buddy and did his master's degree in Italy. From having short catch ups in the campus once in a while and being a thesis-writing buddy, he's been a good encouragement to me. I am grateful for the friendship I built with Benjamin Edun, ever since starting masters at Bilkent together from the next room of the dormitory and journeying all the way throughout. I very much enjoyed playing football with him and discussing about other random topics. I cannot overlook my other football buddies, Davuut and many others. I would like to acknowledge Leo Messi, from whom I have experienced much joy being his big fan over many years.

Special thanks to my close friends, Young and Elliot who have been in touch over the years. I value greatly the friendship we have built especially during the last few years.

I express my ultimate gratitude to my family. My parents have been my physical and spiritual support throughout my studies. They didn't hold back from giving constructive feedbacks to me but at the same time being fully available and present for my needs. I've been able to come this far thanks to their love and sacrifice. I am grateful for my siblings, SH and JH. Just for their presence it gave me comfort and smile. I'd like to mention my extended family, especially my grandparents who cared about me from afar. I extend my profound gratitude and love to ζ, for all the moral support and love I received throughout my masters. Last but not least, I thank God for His guidance, patience, and love.

This thesis was supported by the Scientific and Technological Research Council of Turkey (TÜBİTAK), grant no EEEAG- 116E953.

Contents

List of Figures

List of Tables

Chapter 1

Introduction

Resonance is a phenomenon that is studied extensively in the history of science and engineering, including applications in the filtering of electrical or acoustic waves [1, 2], medical imaging [3], energy transfer in biochemistry [4]. Nano-electromechanical systems (NEMS) are electronically-controlled mechanical structures that have at least the length of a single dimension less than a micrometer [5, 6]. Naturally, due to their size, these structures have great physical sensitivity and can be used as sensors [7–12].

Ever since the first introduction of NEMS [13], there have been many mechanical structures in micro to nanoscale applied to many experiments that explore fundamental phenomena exploiting its exquisite sensitivity, such as thermal conductivity quantization [14], Casimir force measurement [15], ground state cooling, single phonon control of a mechanical resonator [16], and a single spin of electron detection [17]. Also, NEMS applications have been explored by many with their high performances. They include signal processors [18], mass spectrometry [19–21], mechanical logic element [22, 23], and mechanical computers [24, 25].

NEMS devices have been found to reach new limits by having controlled designs. Microwave-range resonances [26] have been discovered, as well as a quality factor(Q) of on the order of a million [27]. One of the reasons for the rapid developments of NEMS technology has been the size reduction of mechanical sensors.

Energy dissipation applications share similar interests with respect to the size of the structures and their quality factors, especially in the field of atomic force microscopy (AFM). In AFM, a big drawback is the slow surface scanning. This limitation stems from having a quality factor that is too high while the resonance frequency is too low, or in other words having a low bandwidth (ω/Q) of the mechanical structure used for scanning. This causes latency for the transient response of the AFM tip to fade away [28] when in high-speed AFM applications accelerating the acquisition rate of each pixel is necessary. Typical mechanical structures used in AFM systems have a dimension of the order of 100 microns. Corresponding structures have a resonance frequency of around a few hundred kHz and a quality factor of around 150. The maximum pixel acquisition rate of a typical AFM is the bandwidth of the mechanical cantilever beam of AFM, which is found as

$$\Omega_{AFM} = f_0/Q = 300kHz/1000 = 300\ Hz.$$

This can be improved by decreasing the quality factor of the mechanical structure at a cost of decreased resolution. For a NEMS sensor with less quality factor and a typical resonance frequency would have,

$$\Omega_{NEMS} = f_0/Q = 15MHz/150 = 100\ kHz$$

which is a difference of close to 3 orders of magnitude. Ideally, a method that can interchange between fast scanning and high-resolution scanning is desired. This can be achieved if the quality factor of the mechanical tip of AFM can be controlled. A way in which this quality factor manipulation is achieved is to have an energy absorption mechanism that is achieved without adding much intrinsic loss to the system (decreasing quality factor with internal friction [28]). A concept of energy sink is a good demonstration of this quality factor control, which is experimented on a larger scale in [29].

However, performing such controlled operations with nanomechanical structures requires precise and quick measurement schemes of the movements. A mechanism developed over the last decade that provides such prompt responses is a method of coupling the mechanical motion to an optical cavity, also called *Optomechanics* [30]. In optomechanical systems motions of nanomechanical structures modulate the optical cavity mode , and thus mechanical motion detection is made possible in the optical regime, providing quick and precise measurement capabilities [31]. Considering a lower frequency regime, coupling of NEMS resonance frequency with GHz range microwave resonant modes can also offer a viable option for fast measurements. This thesis is a work exploring this fast detection mechanism of a resonant mechanical structure, by coupling it to different regimes of electromagnetic waves.

1.1 Thesis Outline

Chapter 1 covers a brief background review of the development of NEMS, and their potential applications in AFM via adjustable quality factors are discussed. With this, the motivation for this work of exploring energy sink mechanisms with optomechanical cavities is addressed.

Chapter 2 explains the process of design parameter optimization and fabrication steps of the optomechanical device.

Chapter 3 discusses about the setup optimization process for light coupling of fiber and waveguide modes. For different combinations of design parameters, various light coupling scenarios are observed and analyzed in terms of the effective coupling strength between the waveguide and the resonator. Then optomechanical device simulations are done for conceptual analysis, and the measurements are performed.

Chapter 4 explores a new design of integrating NEMS into a microwave ring resonator in between the split region with high electric field concentration. The Fabrication of the design is actualized and discussed.

Chapter 5 summarizes the work and suggests the future direction of the work.

Chapter 2

Design and Fabrication

2.1 Fundamental Design

Just as it is for any designing procedure, it is crucial to have a carefully planned fabrication flow with the consideration of feasibility. For instance, in manufacturing a piece of furniture it is important to consider the lengths of the parts, sizes of the holes, and some marginal spaces to fit parts into one another. Similarly, micro-nano fabrication sequences follow similar ideas, but just on much smaller scales. It often flows in a linear sequence of steps of adding or subtracting different layers either to the top or the bottom direction like building blocks. Naturally, alterations in the earlier steps can lead to changes in the parameters of the subsequent procedures or even require revisiting the consideration of the feasibility of the design.

But before designing the fabrication procedures comes *planning* of the device. If the layer designs were blueprints of cars to be built, then the device planning would be considering what type of car it would be at the end of the production. Depending on the goal the designer has in mind, he can turn it into a very different type of car, or within the same category some variations can be added or some existing features can be removed.

The beauty in micro-nanofabrication is that this kind of variation of addition and subtraction of features can be explored collectively. Within one fabrication step, a number of devices can potentially be processed with exponentially increasing numbers as the smaller the size of the devices gets.

2.1.1 Resonator Design

This exact notion of combining different variations in a set is integrated into designing the optomechanical chip. Two types of optical resonator structures are considered for this work. First is the ring resonator, where the radius (R) is the defining variable of the design apart from the dimensions and the materials of the waveguide which are globally held constant within a fabrication step for other devices within the chip. The other one is the racetrack resonator whose variables are the radius (R) and the straight line part (RT). An illustration of this is shown in Figure 2.1.

One other parameter that can be considered is the coupling gap which is the distance between the bus waveguide and the resonator. As the light wave is introduced into the waveguide, due to the difference in index of refraction it travels confined within the waveguide with total internal reflection. However, the electromagnetic field does not terminate at the boundary as it reflects but forms an evanescent field, according to Maxwell's equation. Within the proximity of a few wavelengths of light when another waveguide is introduced, this evanescent field can be coupled and transmitted to this waveguide, a phenomenon called *frustrated total internal reflection.* Thus in order to achieve light coupling, this coupling gap should be kept under a few wavelengths.

In designing the mask of these two types of optical resonators, these parameters were varied but first tested with a few examples using the finite difference time domain (FDTD) method in ANSYS Lumerical software.

The waveguide structures and the resonators are formed from a thin silicon nitride (Si_3N_4) layer on a silicon dioxide (SiO_2) layer with silicon (Si) base chip

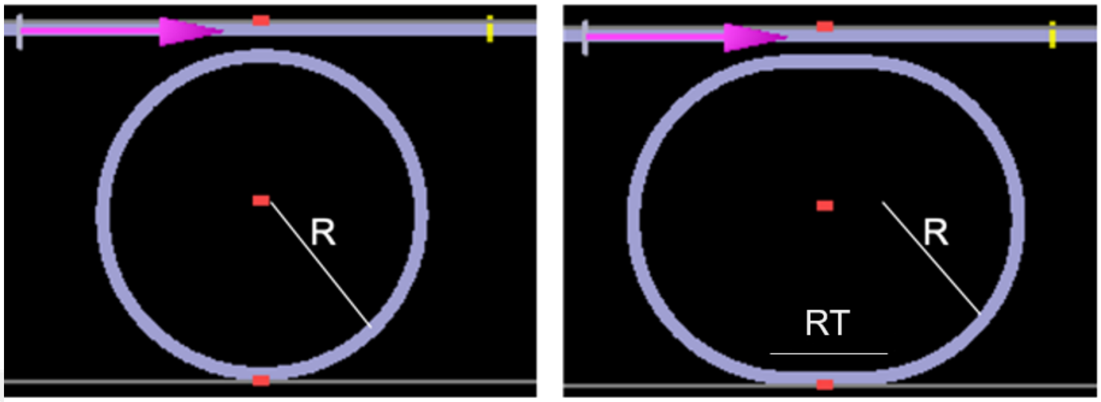

Figure 2.1: A conceptual ring (left) and a racetrack (right) resonator design.

(but for the simulation in designing, it is done in 2D with Si_3N_4 only, as shown in Figure 2.1). A range of electromagnetic wavelengths (765-780 nm) is simulated to optimize the light transmission to the chip. Along with the parameters of the resonators mentioned above (R, RT), the waveguide dimensions and the coupling gap is taken into consideration for optimization in simulation.

A simple resonant condition for ring-shaped resonators has a well-known formula,

$$2\pi r = n\lambda_r, n = 1, 2, ..., \tag{2.1}$$

where r is the radius of the ring and λ_r is the guided resonant wavelength. In the case of an optical wave confined in a waveguide, the change in the wavelength due to light traveling in a medium needs to be taken into account.

The electric field transmission values are investigated with varying parameters of radii 2.3, 3, and 5 μm for ring resonators and racetrack resonators of the same radii with the addition of 1 μm straight section. The coupling gap distance is kept at 200 nm for all configurations. As for the ring resonators, the closest distance from the bus waveguide is taken as the coupling gap, and for the racetrack resonators, the distance between the straight part and the bus waveguide is taken. In the simulation, the resonance wavelength value shown with the largest trough in the light transmission is determined for each configuration. The magenta arrow represents the source of light, and the yellow line represents the transmission data extraction point (see Figure 2.1).

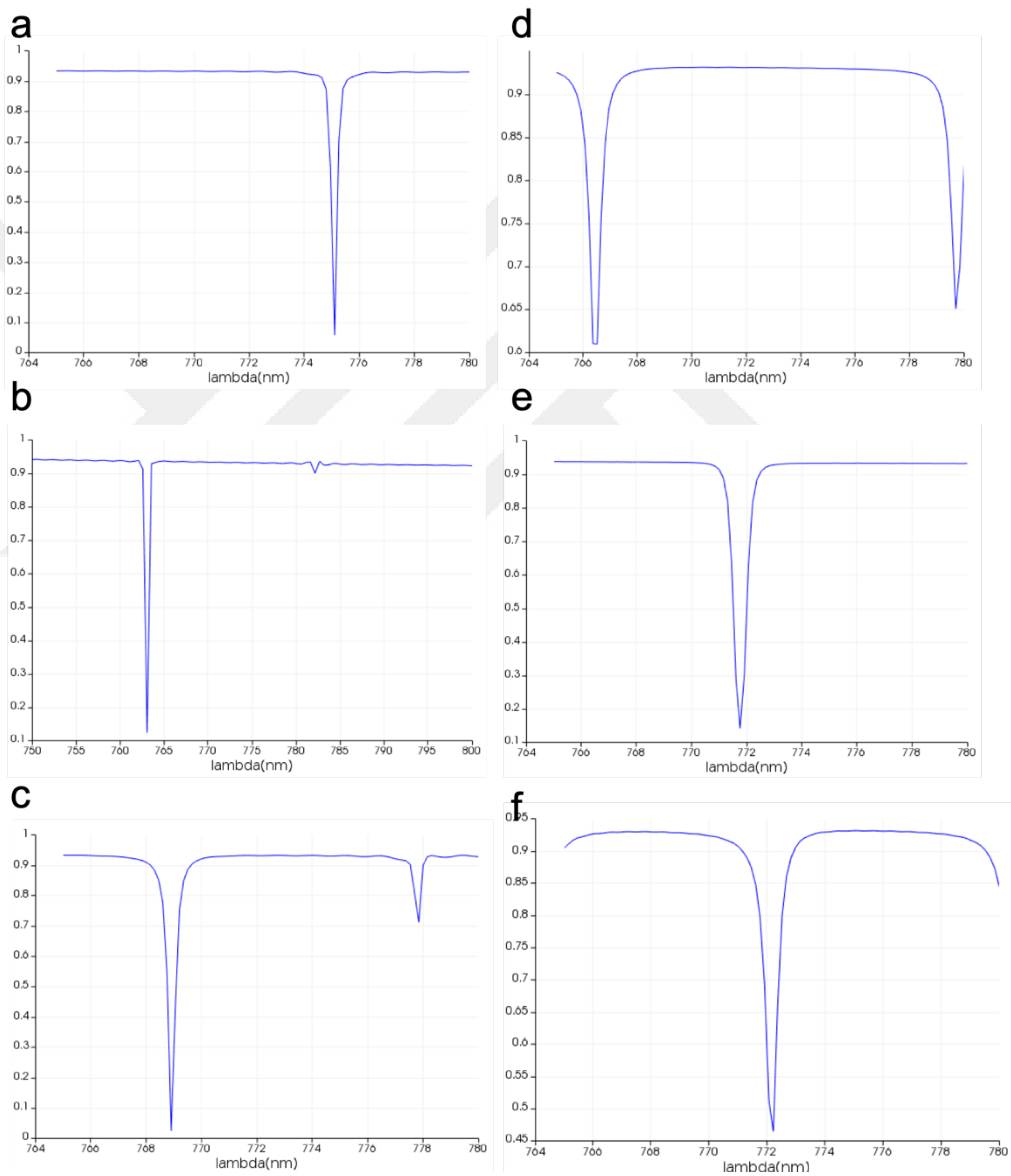

Figure 2.2: EM field transmission simulation plot against wavelength. (a,b,c) the ring resonator configurations with R = 3, 2.3, 5 respectively. (d, e, f) the racetrack resonator configurations with R = 3, 2.3, and 5 respectively.

In all of the designs, there was at least one resonance wavelength detected except for the configuration of the ring resonator with R = 2.3 μm. Some of the configurations had coupling efficiencies greater than 85% (R = 3, 5 μm ring resonator, R = 2.3 μm racetrack resonator, see Figure 2.2).

2.1.2 Grating Coupler Design

There are a few methods of coupling an external light beam into a fabricated chip device. Here in this work, a method of *grating coupling* is chosen to transmit light into the bus waveguide and the resonator, and then to collect the light again after the interaction.

The grating couplers are a structure of periodically spaced elements that are often identical. The most common type is an array of parallel grooves, which is what is used for this work as well. The grating coupler can and often be made of the identical material as the waveguide.

This grating coupler is also simulated with the same software for determining the parameters. The parameters for the grating coupler to decide are the etch depth of the groove (e), the period of the grating defined as the length unit (Λ), and the filling factor defined as the ratio of the un-etched part to the period (FF). For the analysis, the filling factor is set as 0.5, the period as 600 nm, and the total silicon nitride thickness as twice the etch depth ($2e$), as shown in figure 2.3.

Because this simulation is now done in 3 dimensions, the layer of silicon dioxide under the silicon nitride grating waveguides is added to the simulation range. The light travels along the waveguide and as it reaches the grating structures, it scatters with a z-directional wave vector. This analysis is done while varying the etch depth of silicon nitride.

There are two types of analysis performed with the variation of the etch depth. In the first analysis, the fundamental mode data is examined (Figure 2.4b) while in the second analysis electric field scattering data which is the collective data

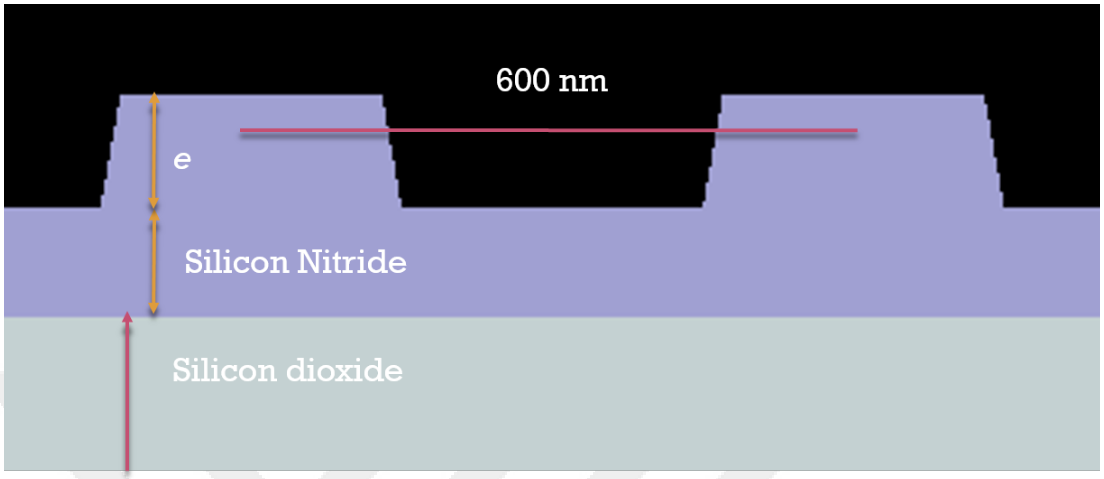

Figure 2.3: grating coupler design for Lumerical simulation.

of several modes. For the fundamental mode analysis, the etch depth of 110 nm is found to be the most efficient in the strength of the scattered light field, but for the electric field mode analysis at 115 nm, the efficiency is found to be at the maximum.

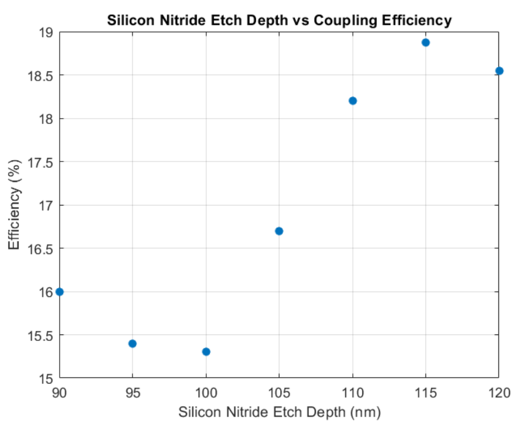

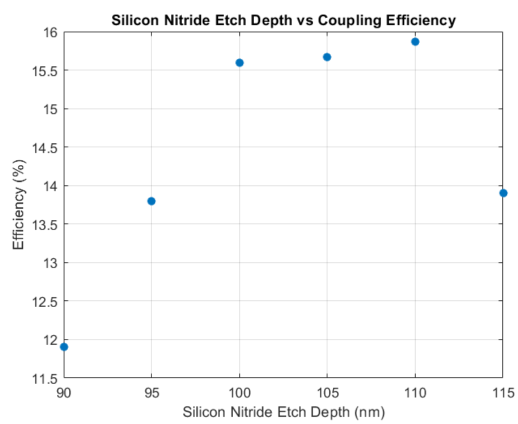

Figure 2.4: Electric field scattering analysis (left), Fundamental mode scattering analysis (right).

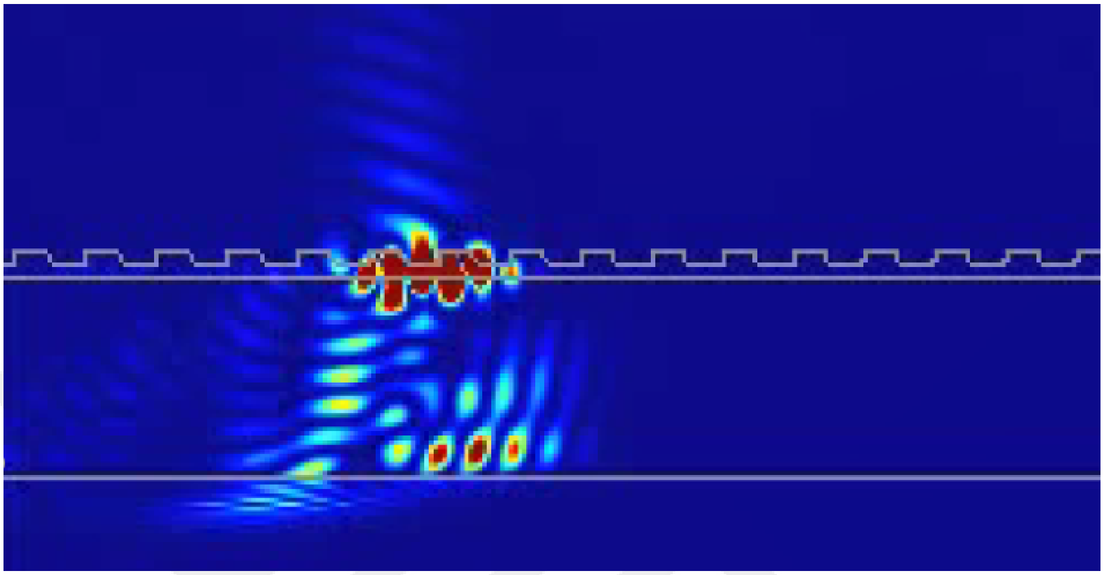

Figure 2.5: Snapshot of light scattering as it travels along the grating structure.

2.2 Fabrication

According to the simulation results discussed in the previous section, the basic parameter dimensions are decided. As for the substrate, the Silicon nitride layer is set as 230 nm to be used in the device (Table 1). Underneath the Si_3N_4 layer, 2.5 μm of silicon dioxide is put as a dielectric layer. Also, variations of device parameters are set as shown in Table 2.2.

	Width	Thickness	Length
Grating structure	27.25μm	115/230 nm	16.12μm
Waveguide	500 nm	230 nm	245 μm

Table 2.1: Dimensions determined for device fabrication.

Ring resonator diameter (D)	Racetrack straight part (RT)	Coupling gap (nm)	Nanomechanical beam length (μm)
5	1	25	6
10	2	50	8
15	3	75	10
19	4	100	12
20	5	125	14
21	6	150	16
25	7	175	18
29	8	200	20
30	9	225	22
31	10	250	24
35	11		26
40			28
45			30

Table 2.2: Dimensions used for the fabrication of optical resonators and nanomechanical devices.

2.2.1 Mask Design

Considering the range of parameters of choice, different combinations of these parameters are designed and drawn as a mask. The GDSII (Graphic Data System) is one of the popular file formats for generating the layers patterns. The matrix of devices is drawn in multiple layers with considerations of different fabrication steps. The mask design used for fabrication is shown in Figure 2.6.

2.2.2 Lithography Steps

There are two main lithography methods widely used in the discipline of micro-nanofabrication: photolithography and electron beam lithography (EBL). For both lithography processes, they share the idea of exposing a pre-coated thin layer called resist on top of the wafer. Then developing the sample into a bath of solution specific to each lithography step will result in the patterns. Depending on the type of resist used for the exposure, either the area of exposure or the

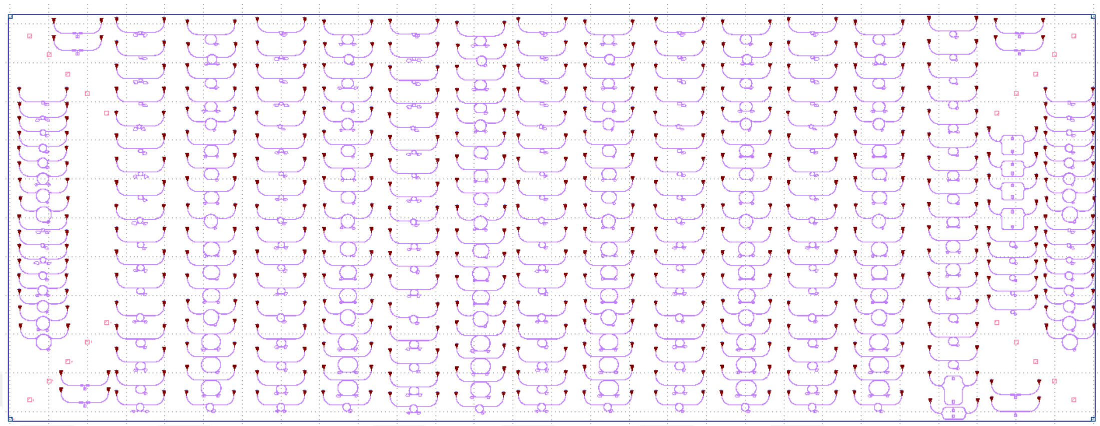

Figure 2.6: A matrix of a multi-layered design file of the optomechanical devices in GDSII format. Each color corresponds to different layers and is used at different steps in the fabrication procedure.

unexposed is dissolved. The resist type of the former is called *positive*, and the latter *negative*. In this work, for both lithography steps the positive type of resists is used.

Photolithography is often useful for creating structures on a bigger scale (>10μm). In a few to sub-micron scale, due to the diffraction limit of $\lambda/2$, it gets increasingly challenging to get good patterning quality.

EBL on the other hand exploits an electron beam in lieu of a photon beam in the case of the other counterpart. This means that the patterning is not limited by the diffraction limit, but only the writefield area used for the exposure. Therefore it is popularly used for fabricating devices on a scale that cannot be reached by photolithography and can reach down to only a few nanometers of feature size. However, the trade-off of EBL being able to create finer structures with higher resolution exists. Often EBL is exponentially more time-consuming with the patterning structure size increasing. It is also encountered that the necessary area dose of electron current to get a good quality patterning results in long scanning time. Additionally, if the fabrication procedure includes aligning to already existing structures, this lithography method often requires a very careful set of alignment techniques and knowledge to perform correctly. For this reason, it is common to consider both methods of patterning depending on the interest of the feasibility, time, and necessity of the fabrication procedure.

As for the interest of optomechanical device fabrication in this work, EBL is the method of choice because of the sub-micron scale features that are included in the device (the waveguide thickness of 500 nm, the grating structures of 300 nm, and the coupling gap ranging from 25 – 250 nm. See Table 1,2).

After the lithography steps, materials are commonly deposited that are either going to be a part of the device structure or as the sacrificial layer before subtracting other layers by the methods of etching. For the optomechanics device fabricated in this work, EBL sessions are performed for a metal layer deposition onto the pattern.

2.2.3 Evaporation and lift-off

Out of many deposition methods that are used in micro-nanofabrication, in this work physical vapor deposition, specifically, *thermal evaporation* is employed. Thermal evaporation consists of a vacuum chamber, thickness monitor (quartz crystal), substrate holder, shutter, and target holder. A desired material is mounted on a boat which is then fixed from both edges of the target holder. From the physical contact of the boat and the target holder, the current is applied to heat up the boat and thus the material to be deposited onto the substrate.

As this is the process of reaching the melting point of the target material, the appropriate boat type should be selected considering its own melting point otherwise would lead to a failed deposition process.

In the optomechanical device fabrication for this work, depositing a sacrificial layer of copper is done using this process. The use of the sacrificial layer is described in the following section.

Once the deposition is done, the sample is put to the liftoff. This process is dissolving the organic resist layer underneath the deposited substance by putting the substrate into an acetone bath. As the resist gets stripped away, the deposited material on top of the resist is removed along with it. And only on the exposed area (unexposed for negative resists) where the resist has already been removed from the development process remains the deposited material.

A rule of thumb for a successful result after lift-off is keeping the deposited material less than a third of the deposited resist thickness. If the deposited material gets thicker beyond this, then it would encapsulate the resist upon which the material sits and the acetone would not be able to reach in between to strip away the resist. Up until this step, the device fabrication is done in collaboration with Dr. Cenk Yanik at Sabanci University.

2.2.4 Etching and Releasing

After a lift-off process, a device would have been constructed with a layer of deposited material or be ready to have a layer removed. If it is the latter case, then the deposited material is called a *sacrificial layer*. The sacrificial layer is used to isolate the underlying substrate by physically covering it with a material that has different properties from the substrate material.

In this work of optomechanical device fabrication, two types of sacrificial layers are deposited on the substrate. The first layer is the aforementioned copper layer, which is used to protect the waveguide structures from etching away while etching the rest of the silicon nitride. This is done in two separate steps in order to create the grating structures. In the first etching step, it forms the grooves at half of the thickness, and in the other step, it forms the full structure of waveguides.

A dry etching method is employed for etching silicon nitride using an inductively coupled plasma etching system (ICP). Because of the way the walls of the waveguide structures are designed to be vertical, the etching needs to be *anisotropic*, meaning the etching is done in a unidirectional manner. The opposite is called *isotropic etching*, which means the etching is non-directional (see Figure 2.7).

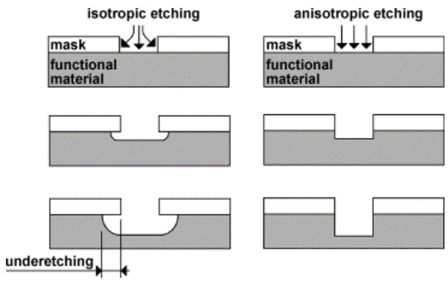

Figure 2.7: Illustration of isotropic and anisotropic etching [32].

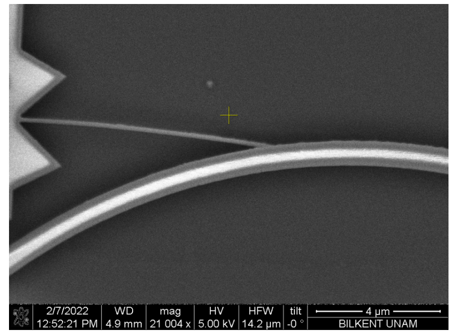

Figure 2.8: Stiction of a Nano-cantilever beam after BOE wet etch.

Another sacrificial layer used is a photoresist layer deposited using a spin coating system. This is used to create an etch window for etching the SiO_2 layer underneath the nanomechanical beams. The etch-window is formed using a standard photolithography process, and the stripped area after the development of the substrate becomes accessible to the etchant, whereas the rest of the substrate is covered by the resist. For this step, the under-etching property of isotropic etching is needed and thus is done with a wet chemical etching method. The process of etching the layer underneath while suspending the top part is called *releasing*. The substrate is put into a Buffered Oxide Etchant (BOE) bath for an optimized amount of time.

One of the caveats of using this method, especially in the fabrication of nanoscale structures, is the structures being pulled down to the substrate or a nearby structure by capillary forces during drying called *stiction* [33]. The devices designed are particularly vulnerable to this effect due to the very close proximity between the mechanical beam and the resonator. This is a very common micro-nanofabrication challenge and also an ongoing research topic [15, 34]. Figure 2.8 shows an occurrence of stiction to one of the device's mechanical beams.

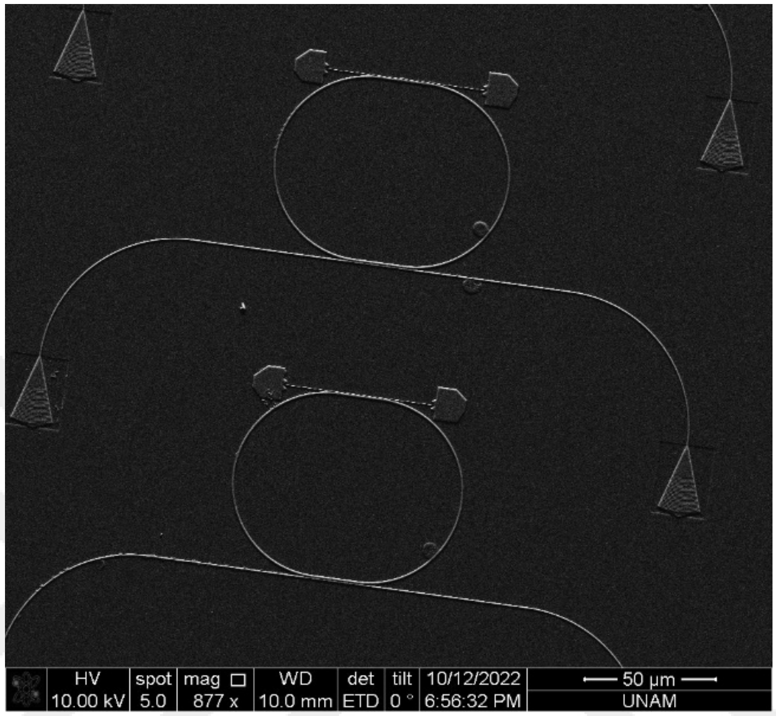

Figure 2.9: Scanning Electron Micrograph(SEM) image of fabricated devices.

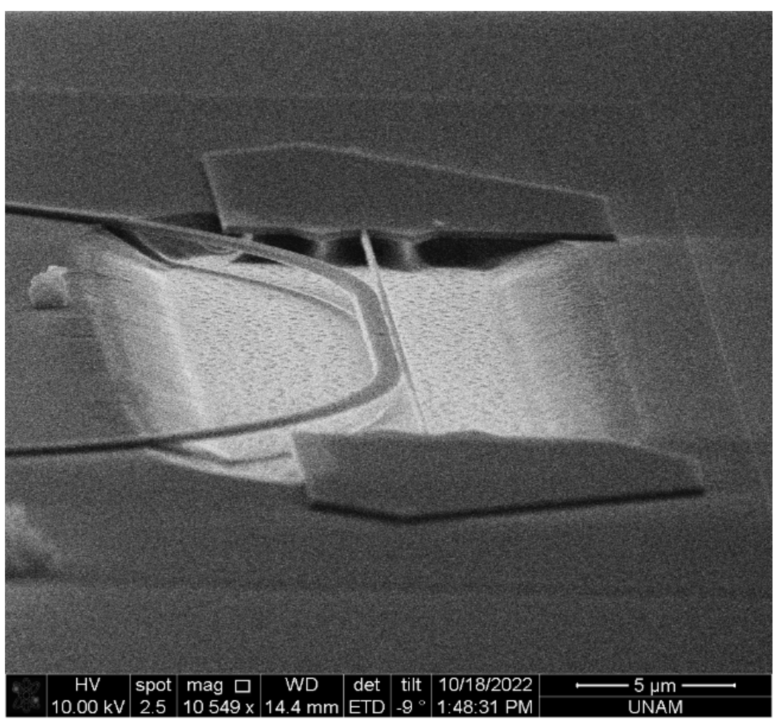

Figure 2.10: SEM image of Etch-released optomechanical device.

Chapter 3

Setup and Measurement

3.1 Setup

3.1.1 Fiber-Waveguide Mode Coupling Investigation

Coupling light into a photonic integrated circuit (PIC) is not a trivial job and needs a carefully examined selection of methods considering its feasibility. Generally, there are two categories of coupling methods; one is called *edge coupling* and the other *vertical coupling*. In the case of edge coupling, the light source is brought from the lateral side and the light is coupled directly into/out from the waveguide, resulting in the same propagation direction. This method stays insensitive to the light polarization and its wavelength and gives high coupling efficiencies ($> 80\%$), but requires great precision in alignment and fine quality of the optical facet on the edge at the wafer. Often, this method requires a tailored edge of the fiber such as a lensed fiber tip to achieve light coupling [35]. Vertical coupling on the other hand brings light from the top onto the chip, and the designed structure modifies the incoming k-vector of the light and guides it into the waveguide. It usually includes diffractive grating structures, and it is marked by relaxed alignment tolerance compared to edge coupling. This method is said to be easier in the fabrication procedure, but instead, its coupling efficiency does not

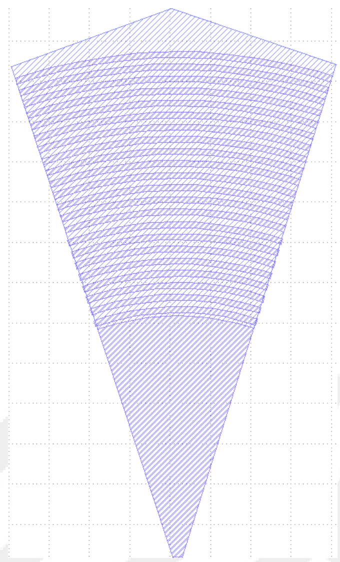

Figure 3.1: Grating coupler mask design.

match the edge coupling option and is sensitive to polarization and wavelength of the incident light [35].

In this work, as discussed in the previous chapter, grating couplers are the method of choice for coupling light to the PIC. The grating structure of our devices has a focusing grating coupler type, where the trenches are curved around the waveguide.

When the angle of the incident beam's k-vector is along the z-axis (perpendicular to the substrate), this is called the resonant configuration. The first mode of diffracted light is vertically emitted from the grating structure, but because the second mode is reflected back towards the waveguide, this configuration is generally omitted in practice. Instead, the k-vector lands at an angle to avoid back reflection. The first-order diffraction angle can be computed from the Bragg condition

$$k_0 \sin\theta_m + mG = \beta_m \tag{3.1}$$

where k_0 is the wave vector of an incident beam, θ_m is the angle between k_0 and the z-axis, m is an integer representing the order diffraction, G is the grating vector, and β_m is the light wave propagating into the waveguide (see Figure 3.2).

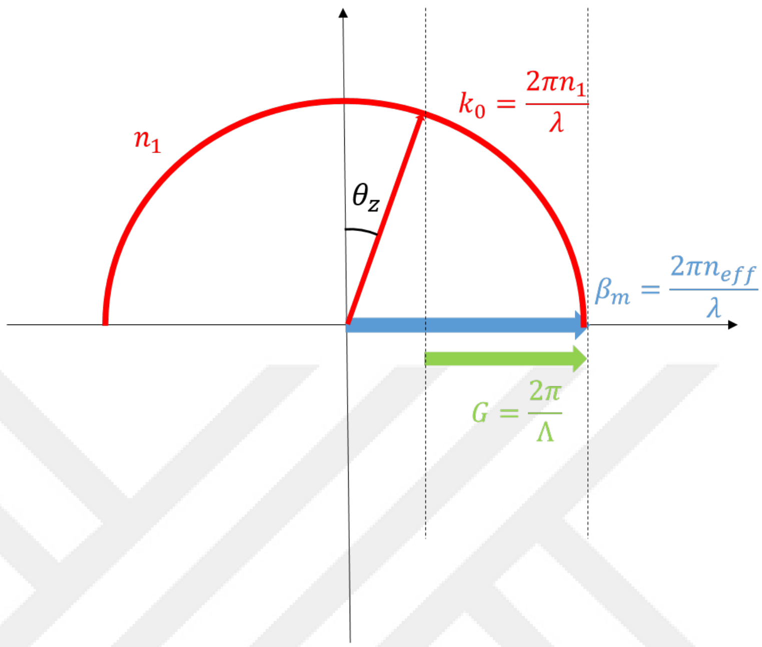

Figure 3.2: Wave-vector diagram for grating couplers.

From the parameters of our design, we find Λ = 600 nm, laser wavelength λ = 770 nm, and a silicon nitride's refractive index at this wavelength. Solving equation (3.1) for θ_m, the first-order diffraction angle is found to be 6.4 degrees.

However, the Bragg condition assumes infinite grating structures and small variations in the index, and in practice, the diffracted beam is not confined in the discrete integer modes but rather forms a bandwidth of diffraction range [36]. This assumption of infinite periods may deviate from the reflection of the realistic scenario [37]. In order to investigate the effective input angle for a more general case, fiber-grating waveguide coupling is simulated in Lumerical software using the FDTD method.

Since the focusing grating type and the straight trench grating have almost identical coupling efficiencies if the etch depths, filling factors (FF), and the period (G) are kept constant, the simulation is done with a straight-trench configuration for its simpler geometric definition. Other than the trench shape, the same parameters listed above are defined. Light is shone at a range of angles and the transmitted electric field strength is monitored.

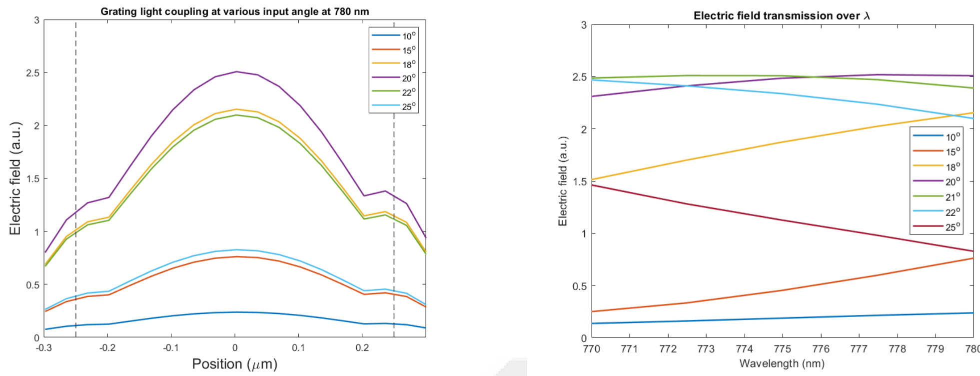

Figure 3.3: (a) Transmitted electric field profile over the waveguide across the width at the center height of the structure at various input angles of light. The dashed line represents the edges of the waveguide. (b) The peak values of the transmitted electric field over the range of wavelength at various input angles.

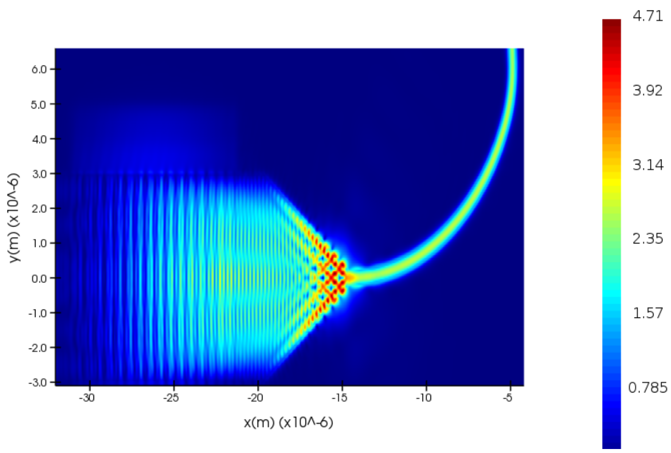

Figure 3.4: Grating simulation plot.

In Figure 3.3b it is shown that within the range of 20 $\sim$ 21 degrees, the monitored electric field is maximal over the range of 770-780 nm of the input wave. This angle is considered in preparing a fiber holder mount discussed below.

Another angle that is needed to be considered is the rotation degree about the Z-axis. Because the distance between the grating structures only being about 250 μm, rotating the holder is inevitable otherwise the fiber tips could not be brought over the gratings at the same time. For this, the ratio of the distance between the two gratings and the minimum clearing distance between the XYZ stage is calculated to avoid the clash of the bulk of the holders. With all the factors taken into account in the design of the 3D printed holder mount, the angles of the mount parameters are shown in Table 3.1.

Rotation about x-axis (°)	Rotation about z-axis (°)
22	3.5

Table 3.1: Fiber mount design angle parameters.

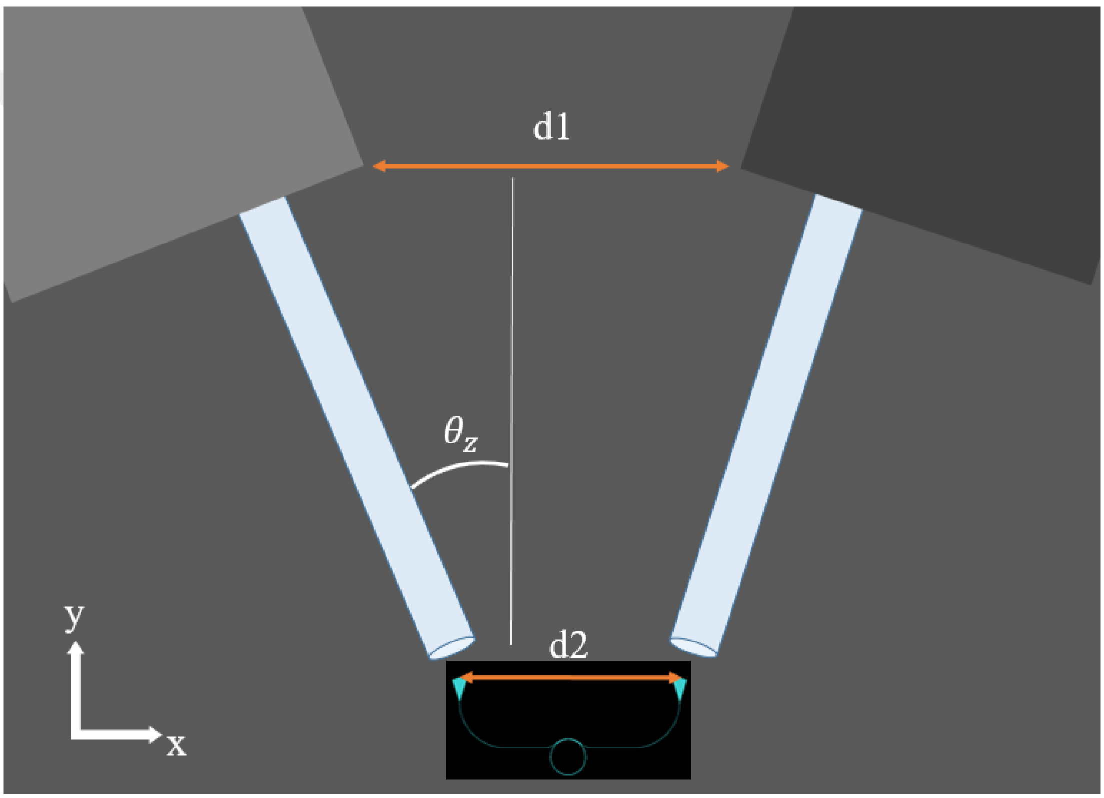

Figure 3.5: A two-dimensional illustration of the fiber holder to Optomechanics device. The drawing is not to scale.

In attempts to make this z-rotation angle as minimal as possible, the fiber holders had to be set back up within the holder mount. This raised another challenge of the fiber holding spot too far away from the grating devices. Even though grating couplers are the less sensitive coupling method, having a long portion of free-standing optical fiber made it vulnerable to random drifts that could completely break the alignment.

To account for this, another piece of fiber holder is introduced to the fiber holding mechanism. Glass slides used for the optical microscope are cut into a

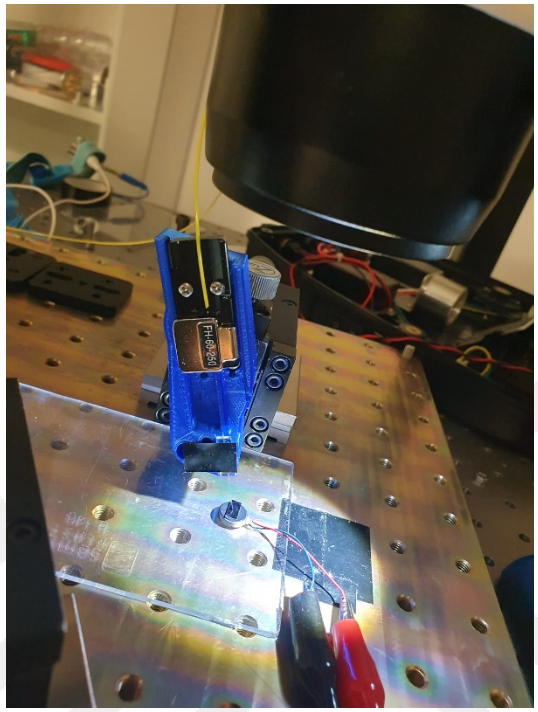

Figure 3.6: Fiber mount design.

small rectangular slab using a dicing saw in the cleanroom setting. On the slab, a narrow groove is made with the depth of the diameter of the fiber.

In order to ensure a good fiber-waveguide coupling, a fine-quality of fiber end facet should be obtained. In this work, Thorlabs ruby fiber scribe unit is employed. The outer coating of the fiber that protects the cladding and the core is stripped and cleaned with isopropyl alcohol (IPA), and the edge of the fiber is cut. The quality of the cut is controlled with an optical microscope. A flat edge shape that is perpendicular is pursued, and the process is repeated until the flat edge is achieved. After the fiber is prepared, it is mounted on the XYZ stages. The setup becomes ready for measurements once all the parts are ready and assembled.

Flowchart of the Fiber-Waveguide Light Coupling

- Fiber coating is stripped with a fiber stripper and cleaned with IPA-dampened fabric.
- Fiber edge is taped on an optical table and gently pulled.
- While maintaining the tension, it is cleaved using a ruby scriber by bringing the scriber perpendicular to the table and rocked on the fiber so that a cutline is formed on the fiber.
- Fiber is pulled and separated from the cut line.
- Check the quality of the surface using an optical microscope. If the tip is slanted or cracked, repeat these steps.
- Fiber is gently mounted and fixed to the stage while making sure the tip is not being touched.
- Place the substrate under the microscope. Ensure that the devices are staying straight and not rotated.
- By rotating the XYZ stage knobs while checking from the computer screen connected to the microscope, bring the fibers close to the devices.
- While the fiber tips are still away from the devices, bring down the fibers until it is observed that the fiber barely touches the substrate. This is done by actually bringing the fiber down slowly and observing it touches the substrate, and bringing it back up. Then the z-axis alignment is settled.
- Turn on the laser power.
- While checking the microscope from the screen, move around the light input fiber over the grating coupler until lighting from the other grating coupler is observed. Try until it shines the brightest.
- Bring the output fiber over the output grating coupler.
- Read the output power measurement from the DC port of the photodetector.
- Rotate the polarization controller pads for the maximum power transmission state.
- Make fine adjustments in the XY direction until the transmission reading is maximized.

3.2 Resonance Measurement and Characterization

The optical signal input is converted into an electronic signal by a photodetector with an operating limit of 1 GHz (NewFocus 1601) into a DC and AC form. Here, the DC port is used for the detection of optical resonance while the AC signal is used for the detection of nanomechanical resonance that is interacting with the optical resonator.

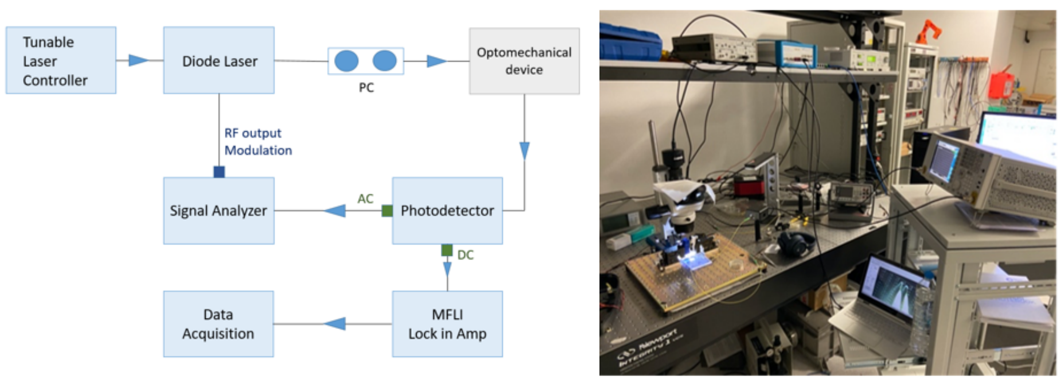

Figure 3.7: A general experimental setup. (a) Light with a diode laser with an operating range of 765-780 nm is polarization controlled (PC) and coupled to the optomechanical devices. The collected light is coupled and sent to a photodetector that has ideal responsivity at around 700-800 nm of electromagnetic wave. The DC output is sent to a phase-sensitive amplifier and the optical resonance data is acquired. For the optomechanical behavior characterization, An RF modulation signal is sent to the diode laser to modulate the frequency of the laser at the MHz range, which is where the resonance frequencies of the nanomechanical beams are located. The modulated signal is sent to the device and fed back to the signal analyzer via the AC output of the photodetector for the measurement of the response.

A series of measurements are done for the fabricated devices for the characterization of the optical resonance for different parameters; the parameters include racetrack length (RT, for the ring resonator this number is omitted), the diameter of the resonator (D), and coupling gap (g). The wavelength of the input laser light is varied at the speed of 0.1 nm/s. With the low pass filter bandwidth(LPFB) of around 20 kHz of the DC port of the photodetector. The LPFB

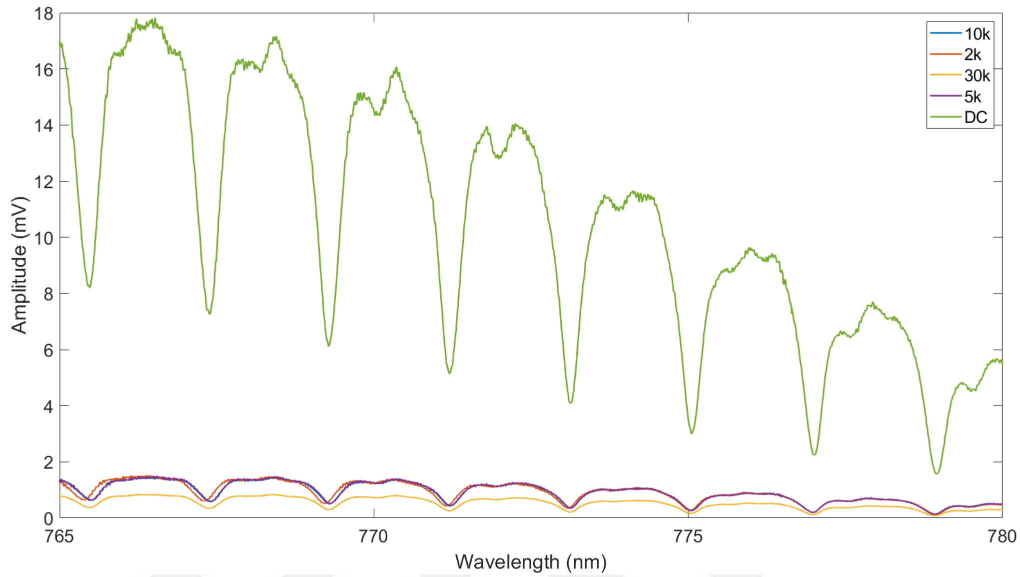

Figure 3.8: Low pass filter test of the measurement setup.

of the measurement setup is tested in Figure 3.8 by modulating the laser output. The cutoff frequency(f_c) of the phase-sensitive detector (lock-in amplifier) stays generally much lower than 20 kHz as shown (1 ms of TC corresponds to $f_c = 160$ Hz).

3.2.1 Resonance Analysis

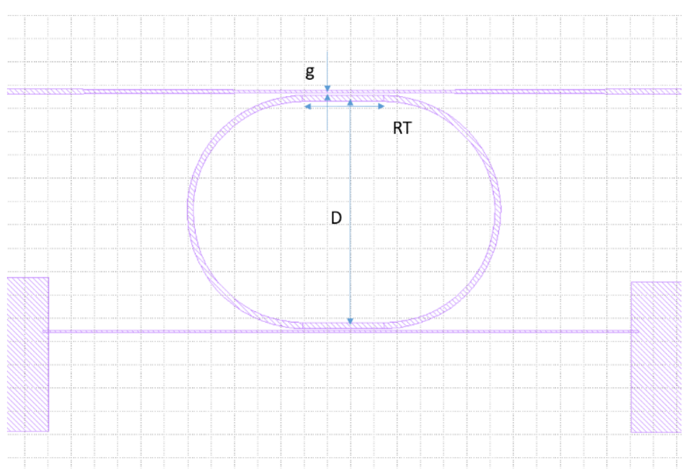

Figure 3.9: Design parameters definition.

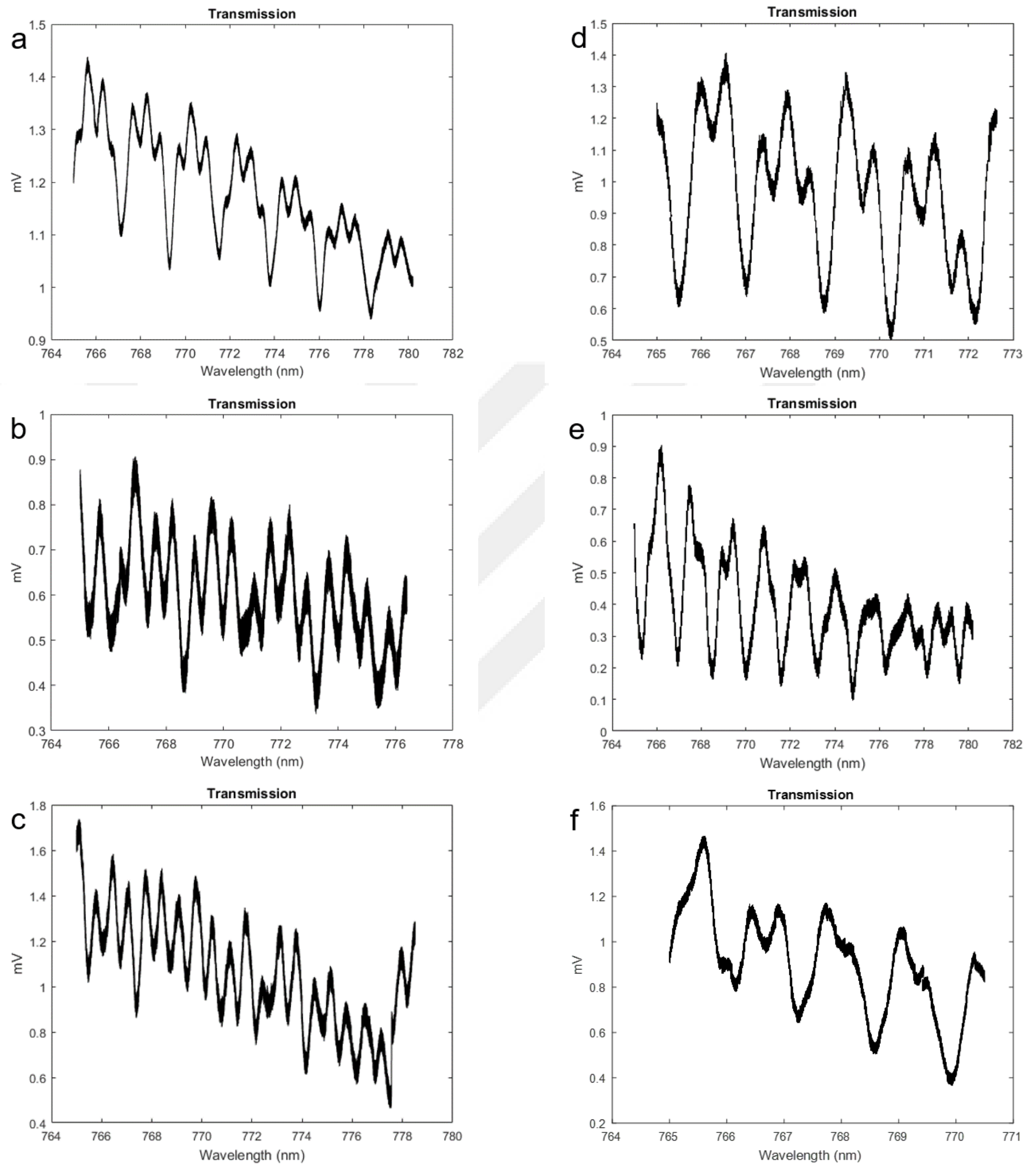

Figure 3.10: Optical readout plots for racetrack resonators with various parameters.

	a	b	c	d	e	f
D (μm)	30	30	30	40	40	60
RT (μm)	10	7	8.7	10	12	12
Gap (nm)	175	175	200	200	200	200

Table 3.2: Design parameters for the racetrack resonator shown in Figure 3.10.

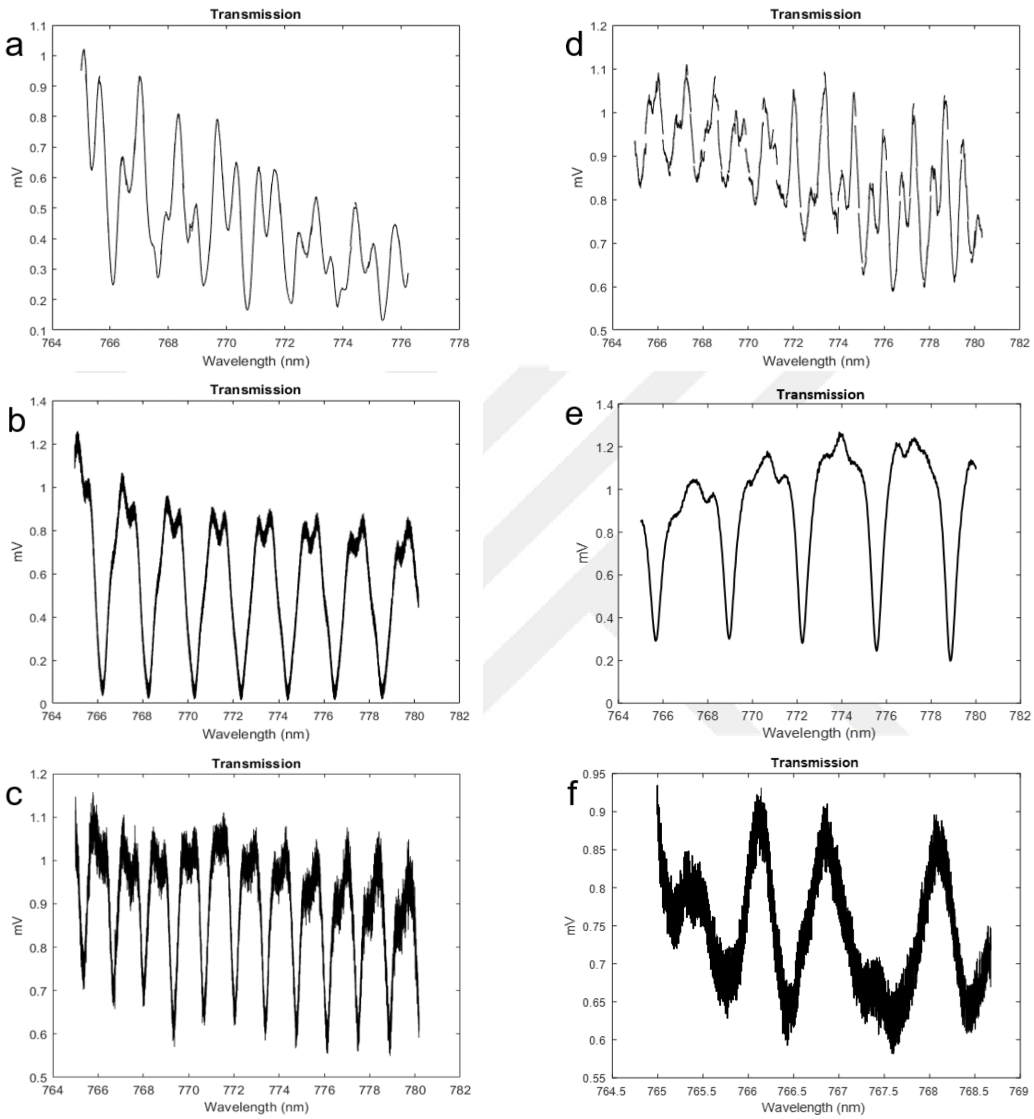

Figure 3.11: Optical readout plots for ring (pulley) resonators with various parameters.

	a	b	c	d	e	f
D (μm)	50	40	60	40	40	80
Gap (nm)	200	225	225	200	175	225

Table 3.3: Design parameters for the ring resonator shown in Figure 3.11.

Here, the optical responses of the devices in different design configurations are shown in Figures 3.10-11 and Table 3.1-2, and the observations are made by comparing the plots that correspond to each configuration. A visual description of each parameter is shown in Figure 3.9.

The following observations are made for the racetrack designs from Figure 3.10

- *b,e,f*; these are some of the cases that are close to critical coupling. The coupling strength is determined by the coupling length (in this case RT) and the gap, which is a crucial parameter to identify the critical coupling configuration. *e*'s contrasts of transmission in the resonance points are the most significant. This is a good indication that *e* is closest to critical coupling out of the candidates. and in this analysis *e* is taken as the main reference for judging the impact of each parameter change from the other response curves.

- *d,e*; without looking at the parameters, one can say *d* has a very similar response to *e*. From the parameter, it is expected that the response of *d* would present undercoupling characteristics compared to *e*. This is shown by the sharp but less amount of amplitude contrast of the resonance dip, albeit small difference. These resonance responses with close parameter settings confirm that this combination is within the range of critical coupling.

- *e,f*; The total length of the resonator waveguide is determined by D and RT. In light propagation via total internal reflection, there's loss innate to the mechanism in the form of an evanescent field. Also, the field strength decays with the absorption by the waveguide material. Thus, with the same coupling strength ($\sim$RT, g) between *e* and *f*, with *e* being close to critical configuration, it is expected that *f* with a longer D would be undercoupled, and this is shown with smaller Q of *f*.

- *a,d*; From *d* to *a*, both the gap and D are decreased. With both enhancing the coupling strength, it is expected that the configuration *a* would be overcoupling. The Q of *a* being less than *d* supports the idea that *a* is not the ideal case. But it is unclear whether this displays overcoupling.

- *a,b,c*; the response of *b* and *c*, compared to *a* have less coupling strength configurations (either less RT and/or more gap). The response plot shows that the two plots are undercoupled.

The following observations correspond to ring design resonators from Figure 3.11. For the ring resonators with pulley waveguides, the angle of the curvature length that contributes to the light coupling is constant. Meaning, the coupling length is proportional to the diameter of the resonator. Thus, the diameter and the coupling length can be considered coupled parameters (the bigger the diameter, the longer the coupling length)

- *b,d,e*; in the comparison of these two plots with good resonances, for the same range of wavelength *e* has a less number of resonance peaks with less quality factor compared to *b* when the same circumference is considered, so in figure 3.11 *b* is set as the reference signal as a critical coupled case. From this, by comparing the parameters one can say that *e* should be an overcoupling scenario. By looking at the extinction ratio of the transmitted light, the coupling gap of 225 nm is a better coupling gap for the pulley-type ring resonators with a diameter of 40 μm. From this, it is clear that *d* does not display a good resonance despite being within the parameter range of *b* and *e*. This suggests that the quality of fabrication is crucial in obtaining good resonance.

- *b,c*; Although both have a series of sharp resonance responses, *c* is slightly more overcoupled compared to *b*, as the Q of the resonance curves are less in *c* than *b* and there are more local oscillations within non-resonant range. This shows that the effect of longer coupling length is greater than propagation loss due to a bigger resonator diameter. Note that the increase in the number of resonances is due to the increase in the resonator length that can fit more sets of wavelengths under the resonance condition.

- *b,f*; one can tell that it is overcoupled compared to *b* due to its longer coupling length from a bigger diameter. This is seen from having less Q and a noisier signal.

- *a,b*; parameters of *a* has a longer coupling length (from larger D) and a smaller gap than the reference plot *b*, therefore overcoupling is expected, which is shown in plot *a*.

In this analysis, the proportional tendency of the enhancement of coupling to a closer gap, a longer coupling length, and a shorter propagation distance is shown for both racetrack and ring resonators. Based on this, some of the critical coupling combinations are selected for the optomechanical measurement devices.

3.3 Optomechanical Measurement

3.3.1 Thermomechanical Motion Readout

After the functionality of the optical resonator design is confirmed, the next experiment in line is the nanomechanical beam resonance measurement. The setup for this experiment is shown in Figure 3.7. The beams are etch-released in a BOE solution and water mixture for etching silicon dioxide underneath. The stiction problem mentioned in chapter 2 generally appeared more on cantilever-type beams due to a higher torque generated from the capillary force. The doubly clamped beams on the other hand remained intact and are mainly chosen for experiments.

The evanescent field forms along the path of the light that is coupled and travels within the optical resonator. In close vicinity, if there is a dielectric object in motion, it changes the effective permittivity of the portion of the waveguide. By definition, the refractive index is

$$n = \sqrt{\epsilon/\epsilon_0} \tag{3.2}$$

The modulation of ϵ results in a change in refractive index n, and this changes the cavity resonant wavelength (shown in equation (2.1)). If the motion of the dielectric object is periodic around the resonant waveguide at a certain frequency

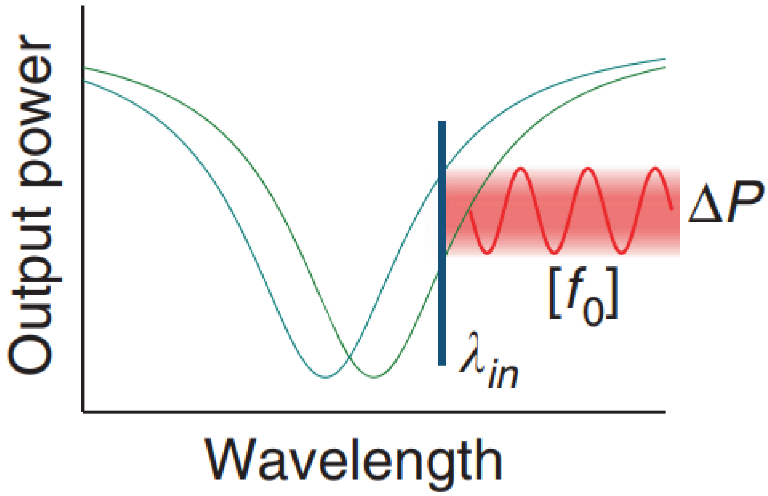

Figure 3.12: Illustration of optical resonance output modulation at the mechanical modulation frequency, taken from [31].

(i.e. mechanical frequency), this modulation frequency information is mixed in the light signal and can be extracted from the output. In order to trigger the nanomechanical signal to be measured, the laser is modulated at a range of frequencies by a signal analyzer output. The expectation is that as the modulation frequency of the signal analyzer coincides with the nanomechanical resonance frequency, the resonance curve appears in the signal analyzer, similar to the idea of frequency component extraction in Fourier analysis. The AC-coupled output of the photodetector has a high pass filter corner frequency of 30 kHz and is connected to the signal analyzer. The expected mechanical beam frequency is in the 1 MHz range (see Appendix A).

While the AC output is monitored for resonance measurement, the DC port measurement is checked simultaneously to ensure optical resonance. The laser frequency is set at a wavelength $dP/d\lambda$ that has some slope but is still close to the resonance dip, because, at the exact wavelength of the resonance point, the frequency modulation created by mechanical movement may not turn into a voltage output (Figure 3.12).

In the curve obtained in Figure 3.13, a dip at around 1.5 MHz is observed. From the analytical calculation of the resonance, with the dimensions

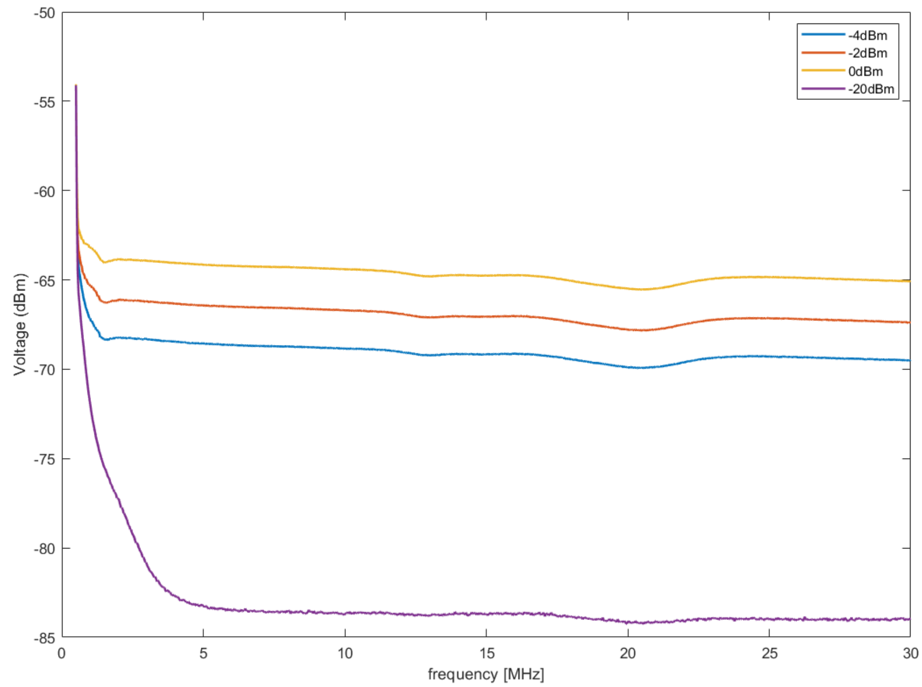

Figure 3.13: Plot of the data received from the signal analyzer. Yellow, red, blue, and purple are response plots with signal analyzer levels 0, -2, and -4 dBm respectively.

of the mechanical beam used the first three modes are 1.59, 4.38, 8.59 MHz ($f_0 = k_n^2\sqrt{EI/\rho A}$). Because the first analytical mode result and the observed value were in close agreement, this was first thought to be the nanomechanical resonance frequency. However, in the following validation experiment, a critical coupling device where the nanomechanical beam has not been etch-released is measured with the same system. As shown in Figure 3.14, the same dip observed at around 1.5 MHz still persisted. The origin of the dips at 13 and 20 MHz is not yet understood. The conclusion from these experiments is that the effect of nanomechanical motion has not been seen.

As the next step, studies on electronic excitation and optical measurement of the nanomechanical structure are discussed. For this, chips with metallic electrodes on the nanomechanical structure will be used.

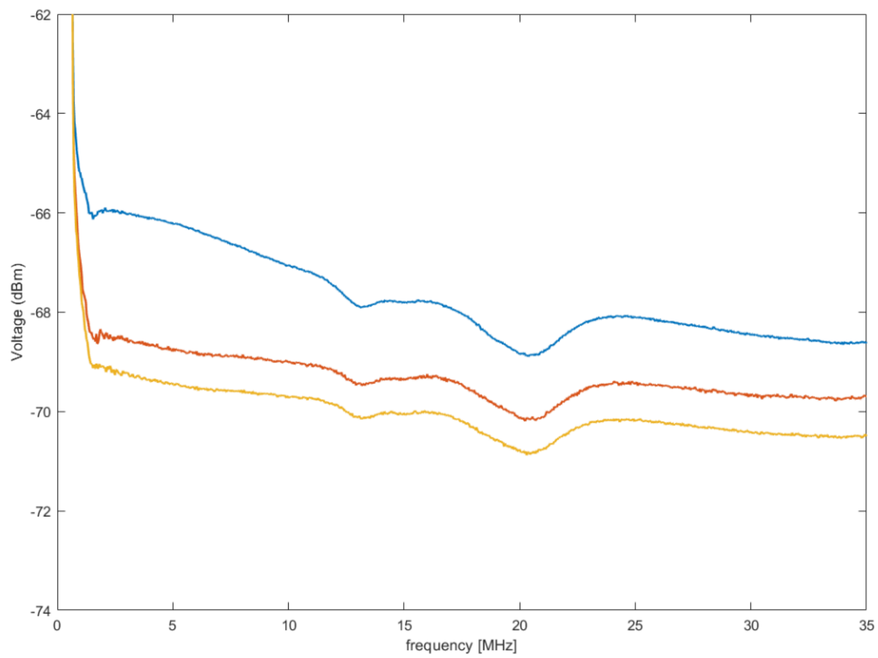

Figure 3.14: Frequency response plot from signal analyzer at different modulation frequencies from a non-suspended, critical coupling device.

3.3.2 Thermoelastically driven Optomechanical Readout

In this section, an optomechanical response from thermoelastic actuation of the Si_3N_4 beams is studied. The main difference in the design is instead of having the Si_3N_4 beams positioned horizontally along the resonating waveguide, they are perpendicularly positioned to it in the form of cantilever beams (See Figure 3.18).

In order to validate the idea and the design, an optical resonator with dielectric substances around is simulated via Ansys Lumerical software using the FDTD method. Since the results were not obtained with the normal optomechanical reading method, simulation analyses are done on the amount of optical wavelength shift that will be made on the optical resonator due to the movement of the mechanical structure during the experiments and how this shift amount will translate into an electronic signal.

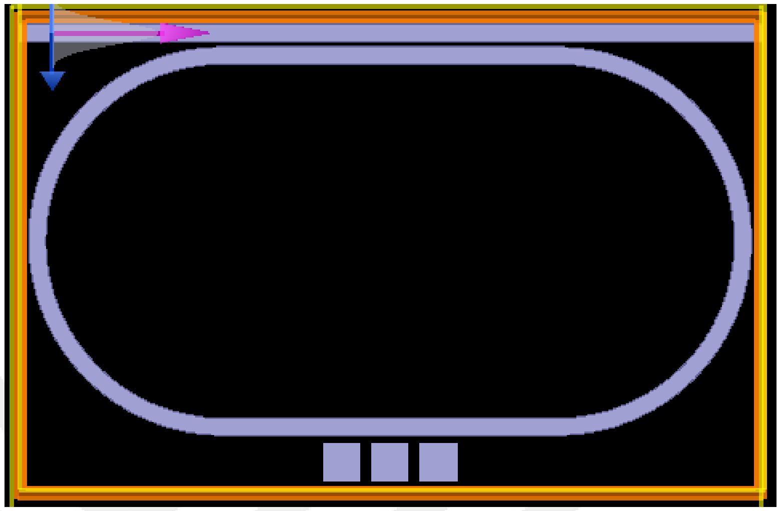

Figure 3.15: Geometry used for the analysis. The three boxes correspond to the tips of the cantilever beams in the experiment.

In Figure 3.15, the simulation geometry is shown. This is a close representation of the actual device used: a racetrack resonator with a three-cantilever beam array of width 1 μm. A series of simulations with a variation of the box (Si_3N_4 cantilever beam) positions out-of-plane and the optical resonance is found for each configuration. The amount of the optical resonant wavelength shift that corresponds to the movement of the beam structures is investigated.

The resonance plots of this simulation are shown in Figure 3.16. In order to estimate the amount of wavelength shift shown in the simulated analysis that would correspond to the actual shift in the experiment, the quality factors (Q) of the simulated and actual resonances are compared. To do this, first, the ratio of the simulated quality factors of the unmodulated and the beam-shifted geometries is computed (50 nm of beam-shift geometry is used). And this ratio is multiplied by the actual resonance's quality factor, and the corresponding resonant wavelength shift is found on the simulated resonance shift (calculation shown in Appendix B). The shifted amount is found to be 3 pm. This amount is interpolated in the actual resonance curve and seen how much voltage shift this wavelength shift corresponds to, and it is found to be 0.25 mV (Figure B.3). Assuming a typical NEMS motion of 5 nm amplitude, it is expected that the signal generated will be in the order of 10 μV according to the simulation results.

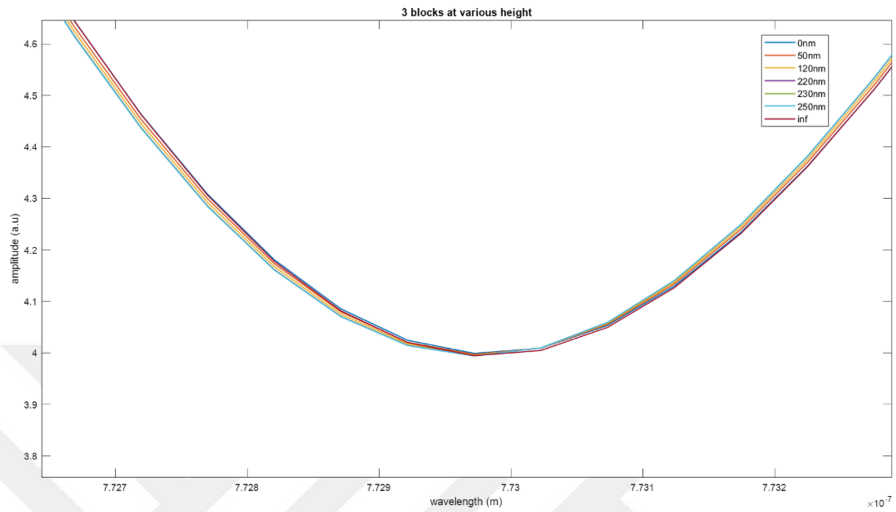

Figure 3.16: Simulated resonance plots.

After the simulation analysis is done, it is moved on to the measurement step. The setup differs from the previous one, as there is thermoelastic actuation. The setup is described in Figure 3.17.

Here, the beam thermoelastic actuation method is used for driving the beams electronically [38]. In this method, an electronic signal of half the nanomechanical resonance frequency is sent to the gold electrodes deposited on top of the nanomechanical structure. Due to the heating-cooling process created by the electric current, the metal expands and contracts periodically. Due to the expansion/contraction movement, a force occurs on the structure at a certain frequency. The frequency of this force occurs at twice the frequency of the applied electronic signal due to Joule heating ($\Delta T \sim V^2$). This expansion/contraction, due to the difference in the thermal expansion coefficients between the gold electrode and the Si_3N_4 beams, the translational movement of the expansion and contraction becomes an oscillation of the cantilever beam in and out of the plane direction. Thus, by applying an electronic signal, it is possible to produce a nanomechanical motion. This motion is expected to create an effect through the optical resonator on the AC output. The resonance frequency range of these beams is 5-7 MHz, simulated via solid mechanics physics module in COMSOL software (Appendix C).

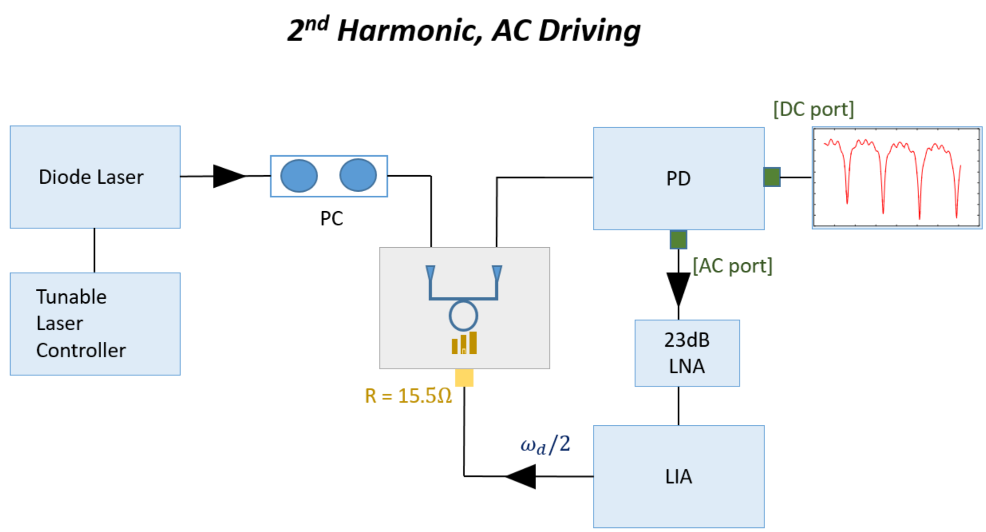

Figure 3.17: The illustration of the setup for optical readout with thermoelastic actuation of an array of beams. From the laser source to the photodetector (PD), the diagram is identical to the previous setup, as well as the DC readout for the resonance wavelength measurement. The lock-in amplifier (LIA) sends a range of driving frequencies to the gold electrode on top of the nanomechanical beams. The electrical current is sent via a wire-bonding technique to the electrode. The light interacting with the resonator and the mechanical beams is collected by the PD, and the AC output of the signal is sent and amplified with a low-noise amplifier (LNA) and fed to the LIA with the data output.

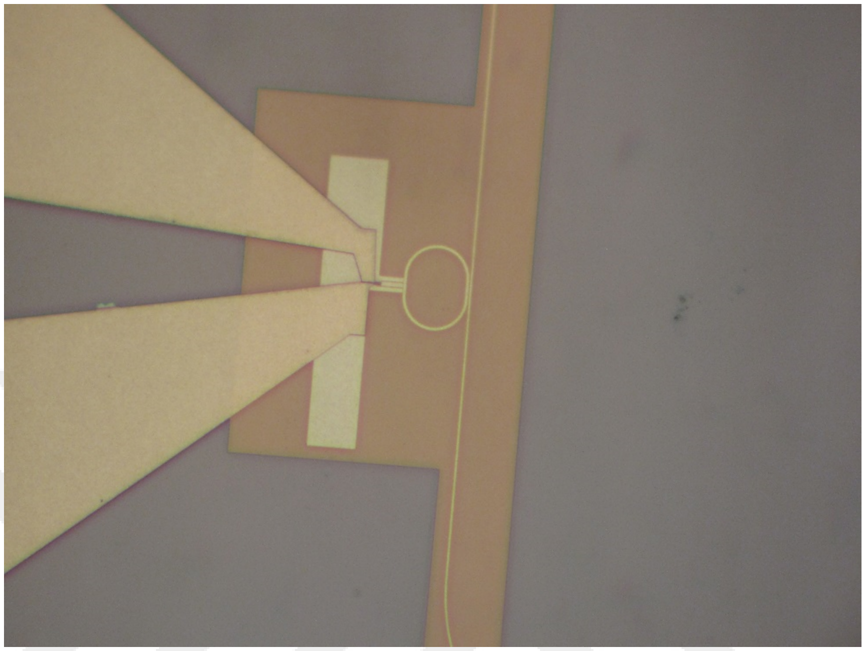

Figure 3.18: Optical micrograph of 3beam optomechanical device.

Under this setup, experiments are performed on devices with good optical resonant quality. In some of the trials, the gold electrode burned due to electrostatic discharge or the high electronic signal to the device. But in two trials, using both pre/post-experiment resistance measurements and post-experiment SEM images, it was confirmed that these electrodes survived successfully throughout the experiment without burning/damaging them. Nevertheless, even though it was scanned with a wide range of 500 kHz to 50 MHz with a high (0.5 – 1 second) lock-in time constant to increase the signal-to-noise ratio, no specific nanomechanical signal was observed (Figure 19-20). To debug the experiment, the functionality of the AC port of the photodetector was tested. It is not understood yet why the nanomechanical signal was observed despite the simulation results.

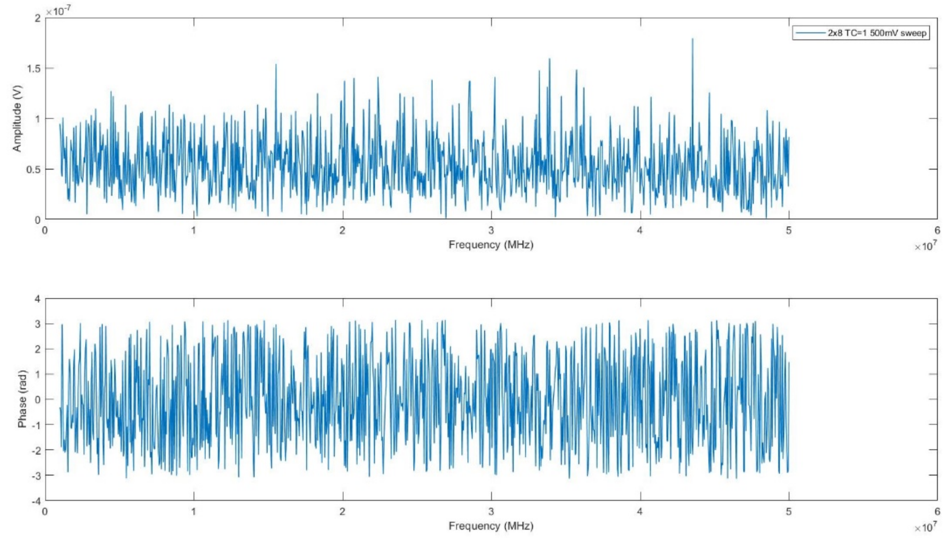

Figure 3.19: Electrical drive, optical readout plot for frequency range 0.5-50 MHz.

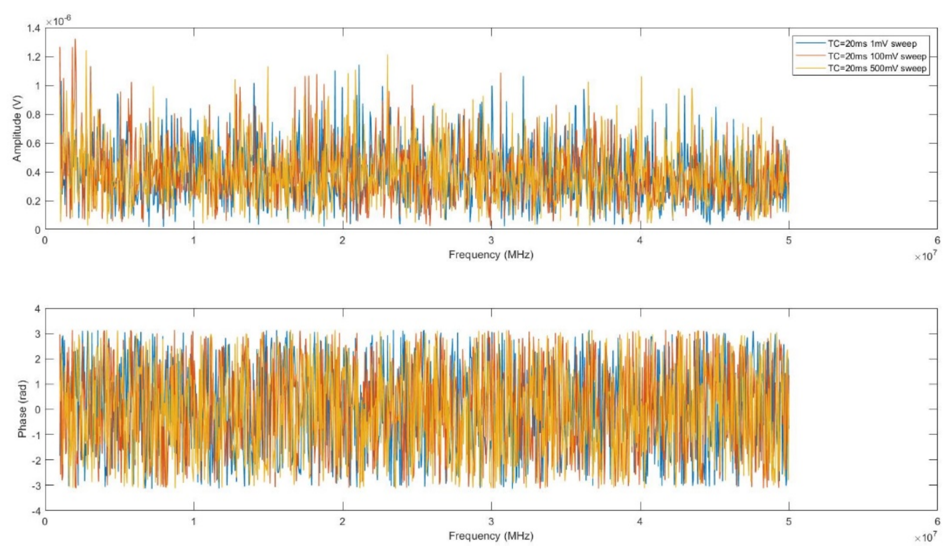

Figure 3.20: Optical readout with three different driving frequencies.

Chapter 4

Microwave Optomechanics Device Design

A new method is explored for the precise detection mechanism of the motion of NEMS in this chapter. Coupling mechanical motion with photons in the microwave domain is already demonstrated in literature [39]. The principle of this mechanism is that the mechanical element's motion capacitively couples to the microwave cavity, modulating the capacitance and thereby the resonance frequency ($\propto 1/\sqrt{LC}$). The key idea of this scheme is to have a very tight coupling gap between the sensing region of the microwave cavity [30]. In this chapter, a new design of placing NEMS in between the gap of a split-ring resonator is studied.

4.1 Concentric Split-Ring Resonator Design Analysis

In estimating the resonance frequency of the ring resonator, the same equation (2.1) used for the optical resonator can be used, where the effective dielectric constant of the substrate modifies the wavelength guided to the resonator. Assuming little contribution of the thin film of silicon nitride to the effective dielectric constant, the resonance frequency of the resonator becomes

$$f = nc\sqrt{\kappa}/2\pi r \tag{4.1}$$

where κ is the dielectric constant of the substrate (for the calculation here, κ of SiO_2 is used, which is 3.8), c is the speed of light in vacuum, and r is the radius of the resonator.

EBL in UNAM has a squared shape chamber, where the maximum length of a sample it can hold is 28 mm. This defines the maximum dimension of the microwave resonator and according to this photolithography mask of 7.5 mm of the radius of the inner ring of a Concentric Split-Ring Resonator (CSRR) design is chosen. Using these parameters, the fundamental resonance frequency of the design is estimated as 3.2 GHz (Mask design shown in Appendix D).

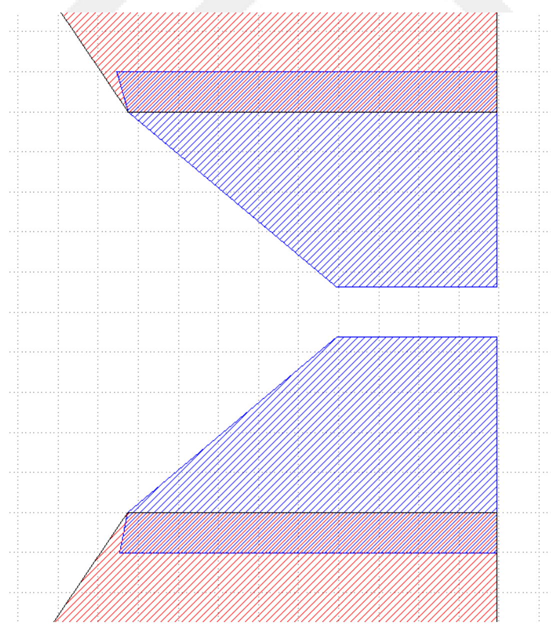

Figure 4.1: Mask design of modified gap size of the CSRR. The red layer is from the photolithography step, and the blue is from the EBL.

However, this is a crude approximation that does not consider the details of the split gap and its width. For a more realistic estimation, the design is simulated by COMSOL via radio frequency module analysis. In the simulation, the thickness of the gold ring that forms the cavity is assumed to be negligible and is defined as a boundary. Similarly, the thin silicon nitride deposited on the fused silica substrate is defined as a boundary. The microwave source is defined as a single lumped port placed in between the gap of the outer ring of the CSRR to represent the S11 measurement setup, where the gold layer of the cavity is assumed to be a Perfect Electric Conductor (PEC). Originally, the split gap of the photolithography mask design is 20 μm. However, this gap is too big for the purpose of microwave photons coupling with mechanical motion and it is truncated using EBL by patterning additional cavity elements to narrow down the gap (Figure 4.1). The design layer of the CSRR is shown in Appendix D.

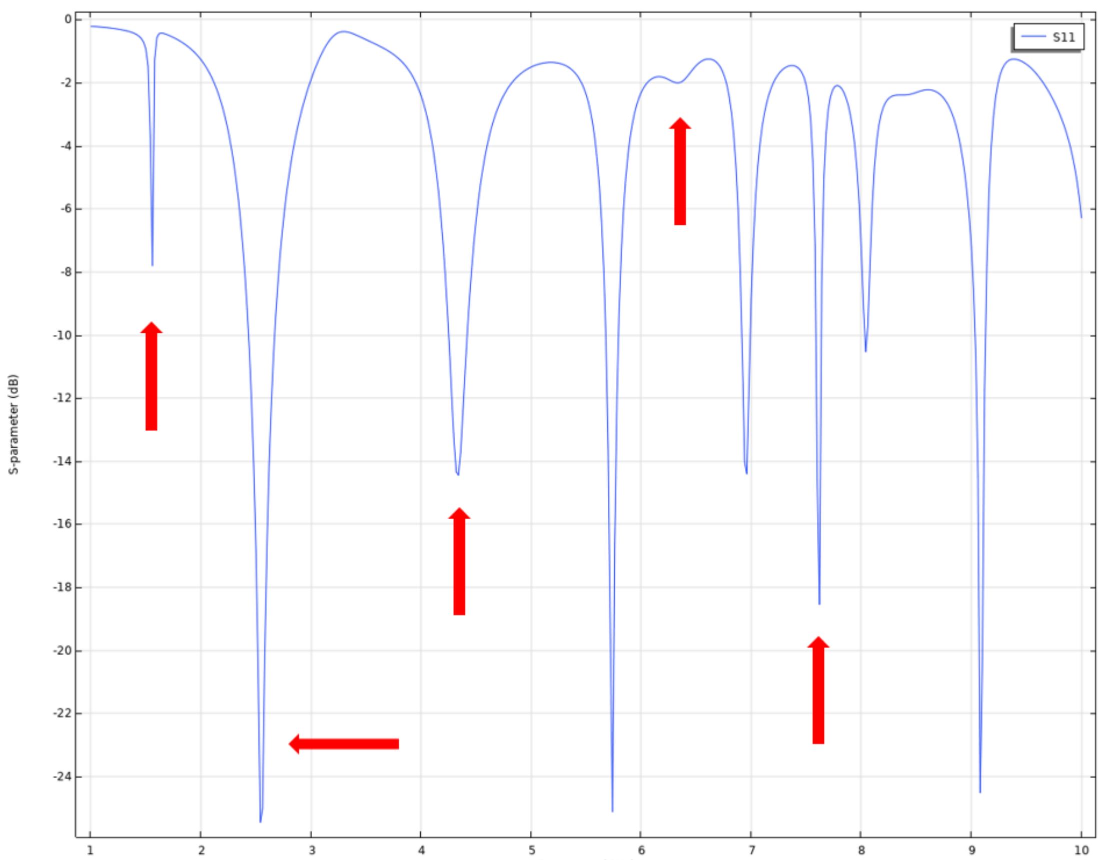

Figure 4.2: The S11 parameter of the CSRR microwave cavity swept over 1-10 GHz with the increment of 20 MHz. The list of the resonance frequencies is 1.56, 2.54, 4.34, 5.74, 6.34, 6.96, 7.6, 8.04, and 9.08 in GHz. The inner ring's resonances are indicated with red arrows.

The simulation result of the S11 parameter is shown in Figure 4.2. There are more than 8 distinct resonance curves appeared in the results. This plot on its own only gives indirect information about the sensitivity of the corresponding resonance frequencies around the sensing gap. In CSRR, because of the two ring resonators of different diameters, there are resonances from both ring cavities. In other words, there are two resonance boundary conditions of the electric field from each cavity, and this is reflected in the S11 parameter field intensity plot shown in Figure 4.2. The sensing gap on the other hand produces high electric field density only with the inner ring resonant condition. The resonances for the inner and outer rings are distinguished by observing the electric field distribution patterns around the cavity (See Figure 4.3), and the inner resonant modes are indicated with red arrows in Figure 4.2.

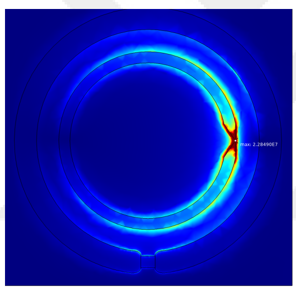

(a) n = 0.5

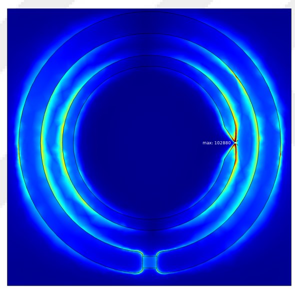

(b) n = 1

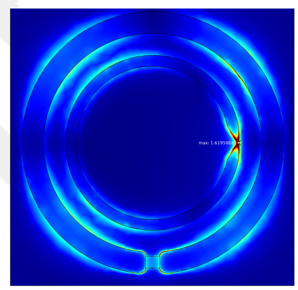

(c) n = 1.5

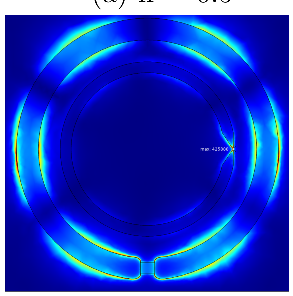

(d) m = 3

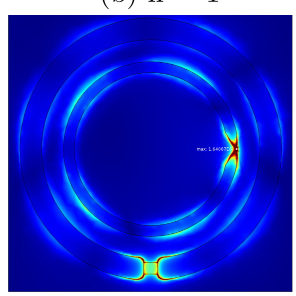

(e) n = 2.5

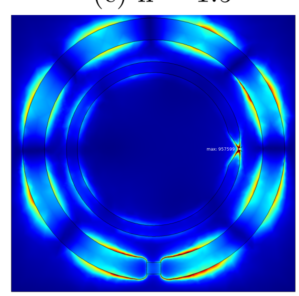

(f) m = 4

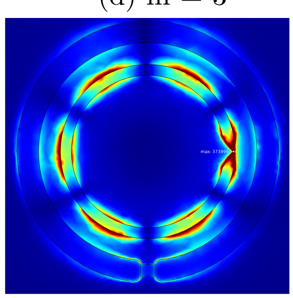

(g) n = 3

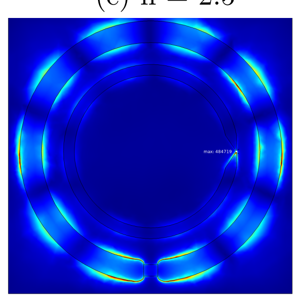

(h) m = 5

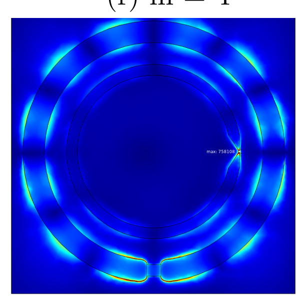

(i) m = 6

Figure 4.3: Resonant mode distribution from COMSOL simulation. n, m denote the resonant mode of the inner and outer ring respectively.

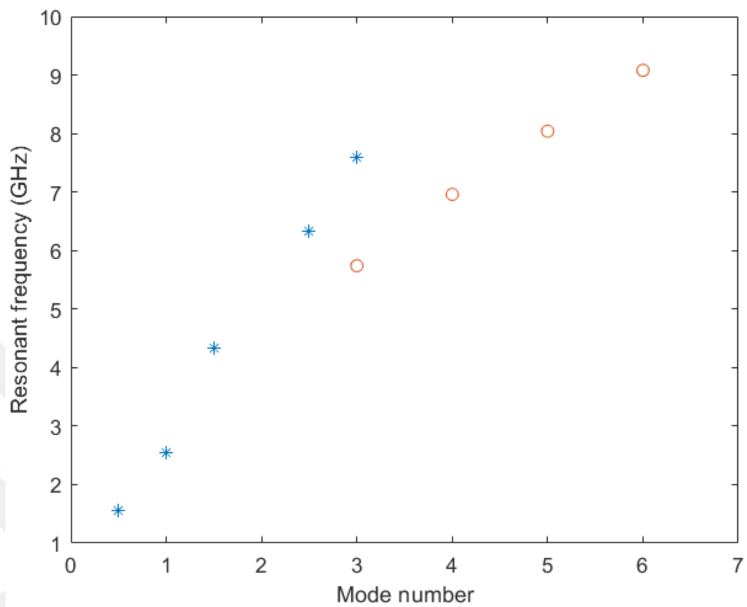

Figure 4.4: Resonant frequency vs mode number of the inner ring (in blue) and the outer ring (in red) of the CSRR.

It is suggested from the field distribution shown in Figure 4.3 that the split resonant modes are observed from the inner ring resonances, as expected from the notch-shaped geometry towards the split and the annular angle of 90 ° between the splits in the outer and inner rings [40]. In contrast, uniform outer ring resonances display ordinary mode numbers of resonance (Figure 4.4). As expected, the inner ring resonant modes possess higher electric field distribution shown by the peak values in Figure 4.3.

4.2 Fabrication

An overview of fabrication is already discussed in chapter 2, and thus the details pertinent to this fabrication process are discussed. This SRR + NEMS device is fabricated in UNAM cleanroom from the beginning.

So far, the CSRRs that are used in our group are fabricated on silicon dioxide wafers. However, for the purpose of the incorporation of NEMS, a new kind of wafer that has a thin silicon nitride film deposited on top of fused silica is selected for this particular design. The wafer is a 500 μm fused silica with 100 nm of silicon nitride with a low pre-stress value.

The bare wafer is cut with a dicing saw at the feed speed of 3, with lengths no less than 26mm and no bigger than 27.5 mm. The first layer of CSRR with a wider gap is fabricated using the photolithography method (PL). A positive resist of AZ 5214 is spin-coated prior to the exposure for 1.6 μm of thickness. It is important in this step to check that at least three of the global alignment markers that are at the corners of the device mask are exposed, which are used in the EBL step as global alignment markers. A thin layer of chromium is used as an adhesion layer before 100 μm of gold deposition. Before every metal deposition step after lithography development, a descum procedure is done using a plasma asher to remove a residual layer of resist on the developed area. After lifting off, a bilayer of PMMA is deposited as discussed in chapter 2 before EBL.

Since the dielectric surface of fused silica and silicon nitride causes charging when an electron beam is shot, fine focusing which is a crucial element for patterning sub-micron structures becomes very difficult without any conductive layer. In this work, 5 nm of a thin chromium layer is deposited onto the PMMA surface. A list of procedures for the EBL in UNAM particular to this work is recorded below:

EBL steps on an insulating surface
(silicon nitride layer on top of fused silica wafer)

- First prepare the sample by following the general spin-coating procedure of e-beam resist (215 nm of 495K A4, 80 nm of 950K A2).
- Deposit 5nm of Cr to form a conductive surface on a dielectric sample. Load the prepared sample into the EBL.
- After performing the patterning, unload the sample and etch the Cr layer with a commercially prepared Cr etchant solution in UNAM cleanroom.
- Develop the exposed layer.

Global Adjustment with alignment marks

- Follow the focusing procedure in [41].
- Find the UV coordinates of the optical photolithography alignment marking positions (or any other well-known location from the first layer of deposition) from the GDS file of the mask.
- Enter them in the 3-point adjustment tab under '*Adjust UV*'. Make sure the setting is Global. To do this, first untick the boxes next to P1, P2, and P3, to be able to edit the positions. Once they are noted, tick the box so that the UV positions that are to be located manually from the SEM are saved. Check from the GDS design if the flags are set at the intended positions.
- From the SEM control screen, find the XY coordinate where the exact UV coordinate is entered into the adjustment tab. Turn on the crosshair to be more precise. Once the image is centered at the location, press the dropper icon to read the XY coordinates. Repeat for all three positions.
- Click *Adjust*.

Local Adjustment with EBL Alignment marks (Second EBL step)

- Make sure that from the GDS design, the manual alignment layer 63 boxes are overlapping on top of the alignment marks. The size of the layer 63 box corresponds to the SEM image screen size.
- Set the writefield to the smallest, but still big enough to capture the alignment marks.
- Drag the design file into a positionlist with layer 63.
- Scan layer 63.
- A scanned image will appear from the Raith screen. By pressing CTRL and pressing the left mouse key, drag the blue crosshair to the alignment mark position. Once it's done, press continue.
- Repeat this for all of the alignment marks.
- After the scan, click accept to adjust the alignment locally within the writefield.
- Repeat this step for better alignment quality.

Global adjustment with alignment marks steps are taken whenever there are already existing patterns from either deposited material. This is meant to align the sample coordinate UV with the stage coordinate XY. However, this is a crude alignment procedure and for pattern alignments that require less than a few micrometer scales, or the pattern is not rotationally symmetric, then *Local adjustment with EBL Alignment marks* steps should be taken. Here, the EBL alignment marks are either pre-deposited or pre-developed patterns from previous EBL sessions. Conventionally, cross-shaped patterns are generated prior to the actual patterning and spaced apart to the corners of an arbitrary square that has the size of the writefield to be used. This can be replaced by any other structures with known coordinate positions in the GDSII file. Preferably, such structures are generated by previous EBL steps for accuracy within a few microns. It is important to note that this manual scanning includes exposing the resist, and it needs to be assured that scanning the marks to be used for alignment does not change the end result.

Ideally, the same writefield size is kept for a single patterning session. However, this often is not the case especially for patterning NEMS structures, because submicron features require tight writefield size whereas for bigger features it is better to use a wider writefield for fast patterning. In order to ensure good stitching quality of patterns generated by different writefields, 'Writefield alignment procedure' shown in [42] is performed for each writefields to be used and checked. The rest of the fabrication steps follow very similar steps to the optomechanical device fabrication discussed in chapter 2. The flowchart of the device fabrication is discussed in Table 4.1,2 below. Also, an image of successful NEMS devices integrated into the CSRR cavity is shown in Figure 4.5.

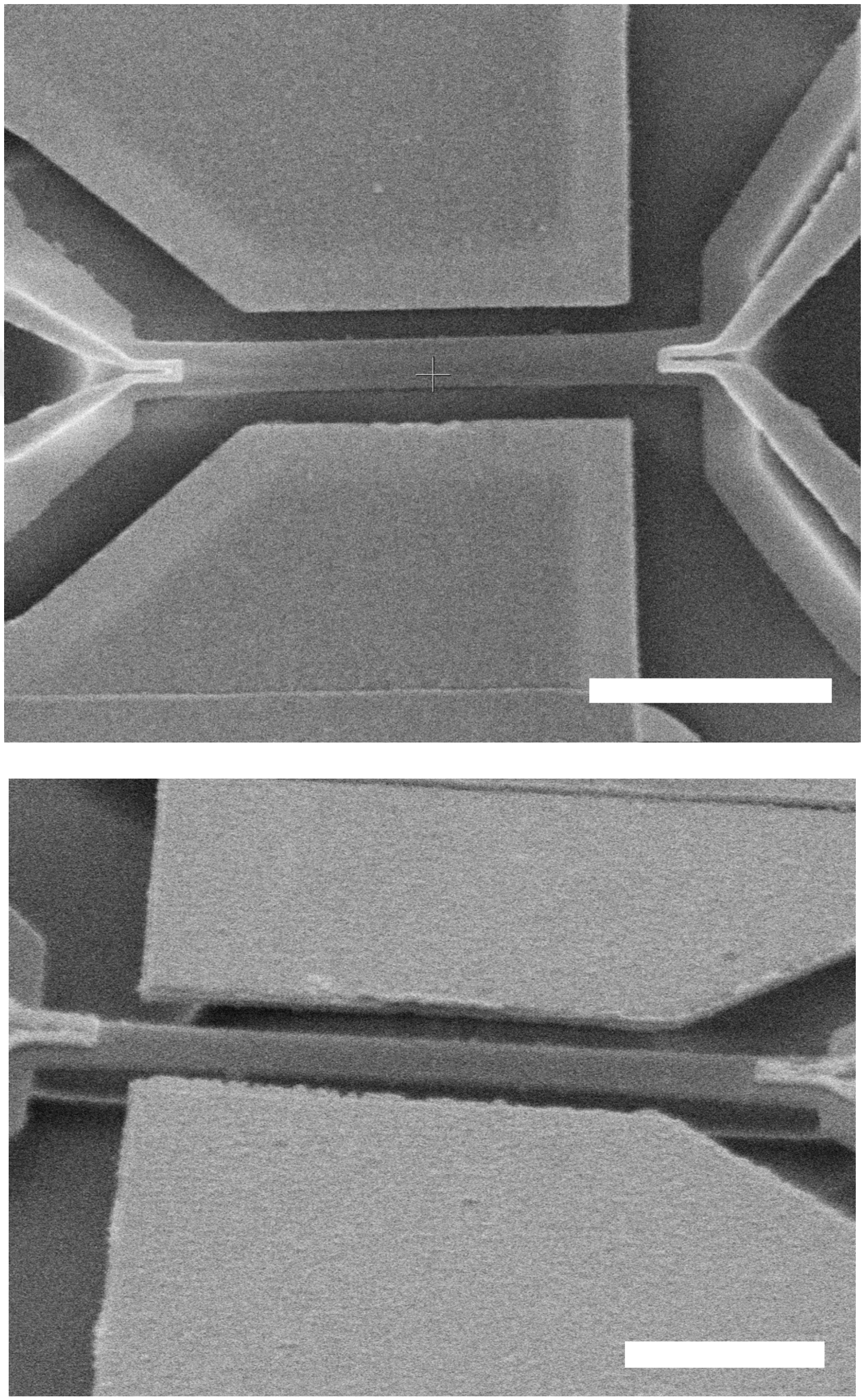

Figure 4.5: Etch-released NEMS device fabricated in between microwave cavity slit. The scale bar is 5μm.

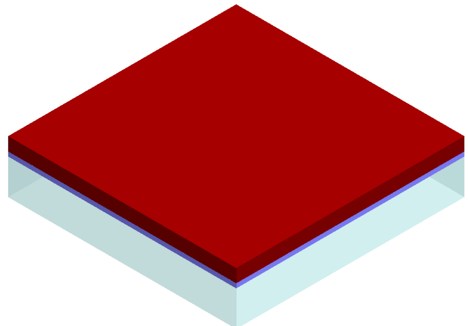	Deposit AZ5214 photoresist on the substrate
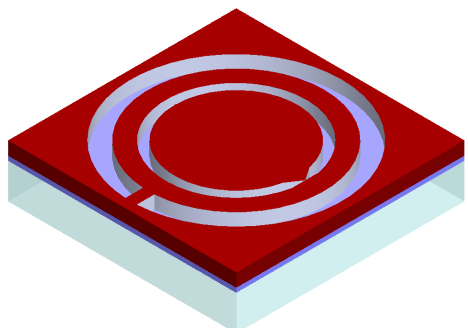	Develop with one part AZ400K developer mixed with three parts of DI water for 30 seconds, and stop the process with water
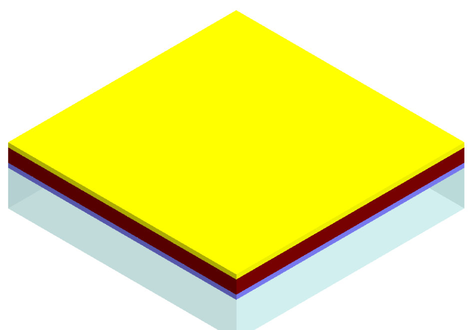	Deposit 100 nm of gold using thermal evaporator
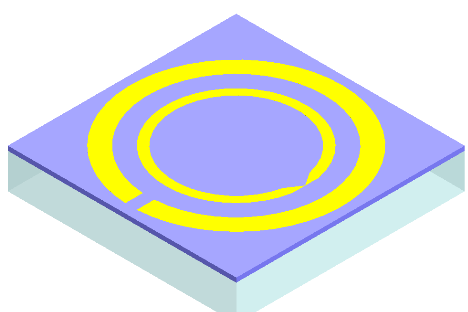	After lift-off in the acetone bath, the microwave gold cavity is patterned onto the substrate

Table 4.1: CSRR fabrication flowchart.

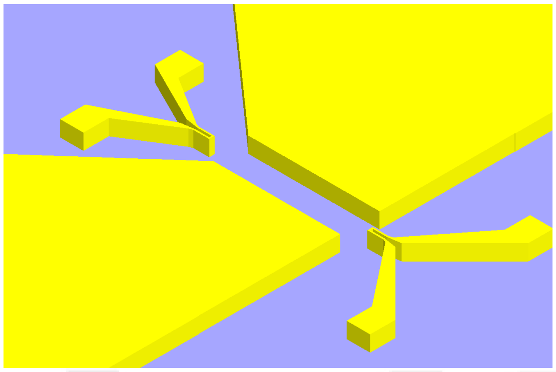	On the substrate with microwave CSRR, deposit bilayer PMMA with 5 nm of *Cr* and follow the guide, *EBL steps on insulating surface.* Deposit 100 nm of gold and perform overnight lift-off in acetone bath
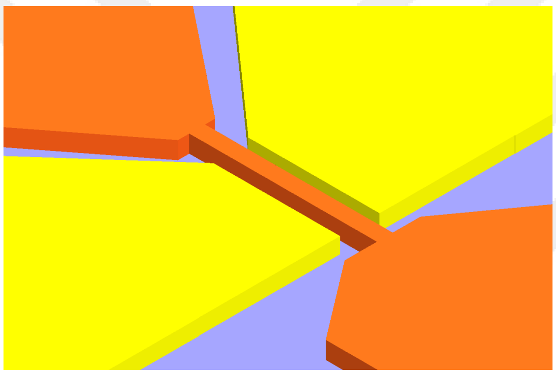	Repeat *EBL steps on insulating surface* with the second layer pattern. Local adjustment is done with manual layer scanning. After the patterning and development, deposit 40 nm of copper and perform lift-off.
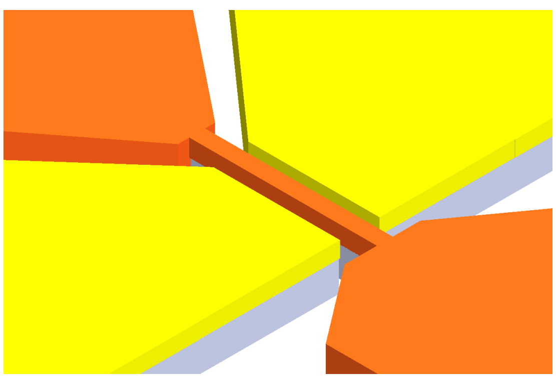	After the liftoff process, Si_3N_4 dry etching is performed, and the SiO_2 underneath the NEMS structure is wet etched with a 1:3 of water to BOE etchant solution for 15 minutes.
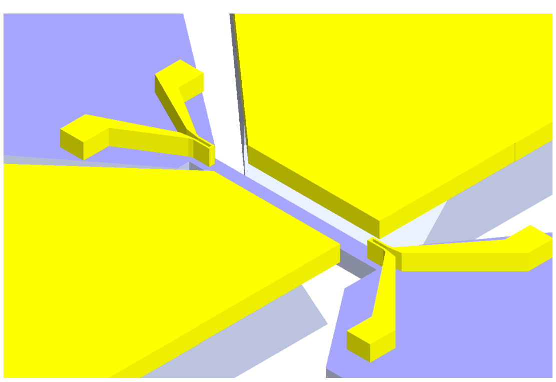	After the releasing step, copper is wet etched with a commercial aluminum etchant solution. Then the device is cleaned with acetone, IPA, and gently dried with N_2.

Table 4.2: Fabrication steps of NEMS in between the microwave CSRR slit.

Chapter 5

Conclusion and Future Work

In this work, two schemes of fast detection of nanomechanical resonant movements are explored via cavity opto-electromechanical coupling in visible light and microwave range. The fabrication methods of both designs are defined. In chapter 2, design parameters for grating couplers are discussed and analyzed with FDTD simulations, and the fabrication methods for the device are explained. In chapter 3 light coupling cases are analyzed with various parameters that affect the coupling strength between the input/output waveguide and the optical resonator. Design optimization for fiber-to-waveguide mode coupling is addressed. Optomechanical readout methods are simulated and shown to be within reach of readout, despite not being seen yet. Microwave range optomechanical device design is done and analyzed in chapter 4. Split modes of concentric split-ring resonators are simulated and shown. A fabrication method for integrating microwave cavity and NEMS devices together is shown to be successful. Especially, design optimization of alignment of material layers generated by both photolithography and EBL is discussed.

Both design schemes have big margins yet to be explored. In the optical readout method, different actuation schemes can be carried out with the measurement, as well as optimization steps carried out in a low-pressure vacuum environment for much-improved signal-to-noise ratio accessibility with higher quality factors.

With recent findings in [19] of the lens focusing of particles, mass spectroscopy can be employed in the optomechanical readout. A protection layer of silicon dioxide to encapsulate the waveguides to be protected apart from the nanomechanical beams is left with an open window with the rest covered with a resist layer. Similar exploration can be done in microwave cavity devices coupled with NEMS.

Bibliography

[1] A. B. Williams and F. J. Taylor, *Electronic filter design handbook*. McGraw-Hill Education, 2006.

[2] D. Morgan, *Surface acoustic wave filters: With applications to electronic communications and signal processing*. Academic Press, 2010.

[3] J. I. C. Hogg, "Magnetic resonance imaging.," *Journal of the Royal Naval Medical Service*, vol. 80 2, pp. 51–4, 1994.

[4] P. G. Wu and L. Brand, "Resonance energy transfer: methods and applications.," *Analytical biochemistry*, vol. 218 1, pp. 1–13, 1994.

[5] H. G. Craighead, "Nanoelectromechanical systems," *Science*, vol. 290, no. 5496, pp. 1532–1535, 2000.

[6] K. Ekinci and M. Roukes, "Nanoelectromechanical systems," *Review of scientific instruments*, vol. 76, no. 6, p. 061101, 2005.

[7] R. Yang, M. Xie, Y. Jia, L. Duraffourg, and P. X.-L. Feng, "Hybrid nanoelectromechanical switch and resistive memory in silicon nanowires by vlsi nems," in *2021 IEEE 34th International Conference on Micro Electro Mechanical Systems (MEMS)*, pp. 607–610, IEEE, 2021.

[8] M. S. Hanay, S. Kelber, A. Naik, D. Chi, S. Hentz, E. Bullard, E. Colinet, L. Duraffourg, and M. Roukes, "Single-protein nanomechanical mass spectrometry in real time," *Nature nanotechnology*, vol. 7, no. 9, pp. 602–608, 2012.

[9] L. M. de Lépinay, B. Pigeau, B. Besga, P. Vincent, P. Poncharal, and O. Arcizet, "A universal and ultrasensitive vectorial nanomechanical sensor for imaging 2d force fields," *Nature nanotechnology*, vol. 12, no. 2, pp. 156–162, 2017.

[10] J. S. Bunch, A. M. Van Der Zande, S. S. Verbridge, I. W. Frank, D. M. Tanenbaum, J. M. Parpia, H. G. Craighead, and P. L. McEuen, "Electromechanical resonators from graphene sheets," *Science*, vol. 315, no. 5811, pp. 490–493, 2007.

[11] K. L. Ekinci, Y. T. Yang, and M. L. Roukes, "Ultimate limits to inertial mass sensing based upon nanoelectromechanical systems," *Journal of applied physics*, vol. 95, no. 5, pp. 2682–2689, 2004.

[12] K. Ekinci, X. Huang, and M. Roukes, "Ultrasensitive nanoelectromechanical mass detection," *Applied Physics Letters*, vol. 84, no. 22, pp. 4469–4471, 2004.

[13] A. N. Cleland and M. L. Roukes, "Fabrication of high frequency nanometer scale mechanical resonators from bulk si crystals," *Applied Physics Letters*, vol. 69, no. 18, pp. 2653–2655, 1996.

[14] K. Schwab, E. Henriksen, J. Worlock, and M. L. Roukes, "Measurement of the quantum of thermal conductance," *Nature*, vol. 404, no. 6781, pp. 974–977, 2000.

[15] H. B. Chan, V. A. Aksyuk, R. N. Kleiman, D. J. Bishop, and F. Capasso, "Nonlinear micromechanical casimir oscillator," *Phys. Rev. Lett.*, vol. 87, p. 211801, Oct 2001.

[16] A. D. O'Connell, M. Hofheinz, M. Ansmann, R. C. Bialczak, M. Lenander, E. Lucero, M. Neeley, D. Sank, H. Wang, M. Weides, *et al.*, "Quantum ground state and single-phonon control of a mechanical resonator," *Nature*, vol. 464, no. 7289, pp. 697–703, 2010.

[17] D. Rugar, R. Budakian, H. Mamin, and B. Chui, "Single spin detection by magnetic resonance force microscopy," *Nature*, vol. 430, no. 6997, pp. 329–332, 2004.

[18] S. Barzanjeh, M. Wulf, M. Peruzzo, M. Kalaee, P. Dieterle, O. Painter, and J. M. Fink, "Mechanical on-chip microwave circulator," *Nature communications*, vol. 8, no. 1, pp. 1–7, 2017.

[19] R. T. Erdogan, M. Alkhaled, B. E. Kaynak, H. Alhmoud, H. S. Pisheh, M. Kelleci, I. Karakurt, C. Yanik, Z. B. Sen, B. Sari, *et al.*, "Atmospheric pressure mass spectrometry of single viruses and nanoparticles by nanoelectromechanical systems," *Acs Nano*, vol. 16, no. 3, pp. 3821–3833, 2022.

[20] A. K. Naik, M. Hanay, W. Hiebert, X. Feng, and M. L. Roukes, "Towards single-molecule nanomechanical mass spectrometry," *Nature nanotechnology*, vol. 4, no. 7, pp. 445–450, 2009.

[21] E. Sage, A. Brenac, T. Alava, R. Morel, C. Dupré, M. S. Hanay, M. L. Roukes, L. Duraffourg, C. Masselon, and S. Hentz, "Neutral particle mass spectrometry with nanomechanical systems," *Nature communications*, vol. 6, no. 1, pp. 1–5, 2015.

[22] S. C. Masmanidis, R. B. Karabalin, I. De Vlaminck, G. Borghs, M. R. Freeman, and M. L. Roukes, "Multifunctional nanomechanical systems via tunably coupled piezoelectric actuation," *Science*, vol. 317, no. 5839, pp. 780–783, 2007.

[23] S. O. Erbil, U. Hatipoglu, C. Yanik, M. Ghavami, A. B. Ari, M. Yuksel, and M. S. Hanay, "Full electrostatic control of nanomechanical buckling," *Physical review letters*, vol. 124, no. 4, p. 046101, 2020.

[24] M. L. Roukes, "Mechanical compution, redux? [nanoelectromechanical systems]," *IEDM Technical Digest. IEEE International Electron Devices Meeting, 2004.*, pp. 539–542, 2004.

[25] F. Chen, H. Kam, D. Markovic, T.-J. K. Liu, V. Stojanovic, and E. Alon, "Integrated circuit design with nem relays," in *2008 IEEE/ACM International Conference on Computer-Aided Design*, pp. 750–757, IEEE, 2008.

[26] X. M. Henry Huang, C. A. Zorman, M. Mehregany, and M. L. Roukes, "Nanodevice motion at microwave frequencies," *Nature*, vol. 421, no. 6922, pp. 496–496, 2003.

[27] S. S. Verbridge, H. G. Craighead, and J. M. Parpia, "A megahertz nanomechanical resonator with room temperature quality factor over a million," *Applied Physics Letters*, vol. 92, no. 1, p. 013112, 2008.

[28] J. D. Adams, B. W. Erickson, J. Grossenbacher, J. Brugger, A. Nievergelt, and G. E. Fantner, "Harnessing the damping properties of materials for high-speed atomic force microscopy," *Nature nanotechnology*, vol. 11, no. 2, pp. 147–151, 2016.

[29] A. Akay, Z. Xu, A. Carcaterra, and I. M. Koç, "Experiments on vibration absorption using energy sinks," *The Journal of the Acoustical Society of America*, vol. 118, no. 5, pp. 3043–3049, 2005.

[30] M. Aspelmeyer, T. J. Kippenberg, and F. Marquardt, "Cavity optomechanics," *Reviews of Modern Physics*, vol. 86, no. 4, p. 1391, 2014.

[31] M. Sansa, M. Defoort, A. Brenac, M. Hermouet, L. Banniard, A. Fafin, M. Gely, C. Masselon, I. Favero, G. Jourdan, *et al.*, "Optomechanical mass spectrometry," *Nature Communications*, vol. 11, no. 1, pp. 1–7, 2020.

[32] D. Li, *Encyclopedia of microfluidics and nanofluidics.* Springer Science & Business Media, 2008.

[33] N. Tas, T. Sonnenberg, H. Jansen, R. Legtenberg, and M. Elwenspoek, "Stiction in surface micromachining," *Journal of Micromechanics and Microengineering*, vol. 6, no. 4, p. 385, 1996.

[34] W. Townsend and J. Salisbury, "The effect of coulomb friction and stiction on force control," in *Proceedings. 1987 IEEE International Conference on Robotics and Automation*, vol. 4, pp. 883–889, IEEE, 1987.

[35] R. Marchetti, C. Lacava, L. Carroll, K. Gradkowski, and P. Minzioni, "Coupling strategies for silicon photonics integrated chips," *Photonics Research*, vol. 7, no. 2, pp. 201–239, 2019.

[36] L. Cheng, S. Mao, Z. Li, Y. Han, and H. Fu, "Grating couplers on silicon photonics: Design principles, emerging trends and practical issues," *Micromachines*, vol. 11, no. 7, p. 666, 2020.

[37] Y. Tang, *Study on electroabsorption modulators and grating couplers for optical interconnects*. PhD thesis, KTH Royal Institute of Technology, 2010.

[38] M. Li, H. X. Tang, and M. L. Roukes, "Ultra-sensitive nems-based cantilevers for sensing, scanned probe and very high-frequency applications," *Nature nanotechnology*, vol. 2, no. 2, pp. 114–120, 2007.

[39] C. Regal, J. Teufel, and K. Lehnert, "Measuring nanomechanical motion with a microwave cavity interferometer," *Nature Physics*, vol. 4, no. 7, pp. 555–560, 2008.

[40] K. Chang and L.-H. Hsieh, *Microwave ring circuits and related structures*, vol. 156. John Wiley & Sons, 2004.

[41] A. B. Ari, "Design, fabrication, and applications of multi-mode nanoelectromechanical systems," Master's thesis, Bilkent University, 2017.

[42] M. Rodder, "Raith ebl guide 2018." https://wikis.utexas.edu/display/wasserman/Raith+Operating+Procedures.

[43] A. N. Cleland and M. L. Roukes, "Noise processes in nanomechanical resonators," *Journal of applied physics*, vol. 92, no. 5, pp. 2758–2769, 2002.

Appendix A

Eigenfreuency Calculation

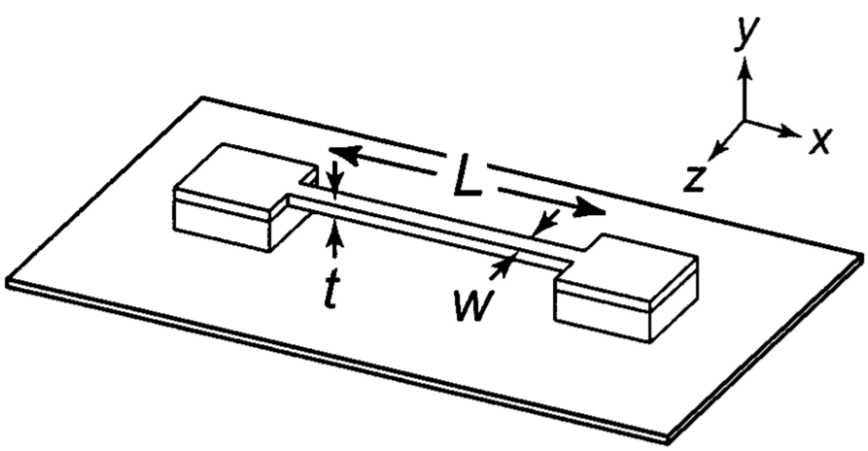

Figure A.1: Doubly clamped beam illustration [43]

$$\rho A \frac{\partial^2 Y}{\partial t^2} = -\frac{\partial^2}{\partial x^2(x,t)} EI \frac{\partial^2 Y}{\partial t^2(x,t)} \tag{A.1}$$

Where ρ is material density, $A = wt$ the cross sectional area, E is young's modulus, and $I = \frac{wt^3}{12}$ is the bending moment of inertia. Since the beam of interest is the double clamped, it has the boundary conditions of

$$Y(0) = Y(L) = 0 Y'(0) = Y'(L) = 0 \tag{A.2}$$

The differential equation with the given boundary conditions has the solutions of

$$Y_n(x,t) = (C_{1n}\cos(k_n x) - \cosh k_n x + C_{2n}\sin k_n x - \sinh k_n x)e^{-i\Omega_n t} \tag{A.3}$$

with boundary conditions, the eigenvectors $_n$ are solutions of $\cos k_n L \cosh k_n L = 1$ The first four eigenvectors are found as k_nL = 4.73004,7.8532,10.9956,14.1372 [43].

$$\Omega_n = k_n^2\sqrt{\frac{EI}{\rho A}} \tag{A.4}$$

Converting to our relevant frequency unit of Hz, first 3 four frequencies of our doubly clamped beam with critical coupling are (L = 37.5 μm):

$$f_1 = 1.59, f_2 = 4.38, f_3 = 8.59[MHz] \tag{A.5}$$

Appendix B

Resonance Shift Calculation

Quality factor ratio change is

$$r = \frac{Q_{shift}}{Q} = \frac{351.557}{351.5584} = 0.999996 \tag{B.1}$$

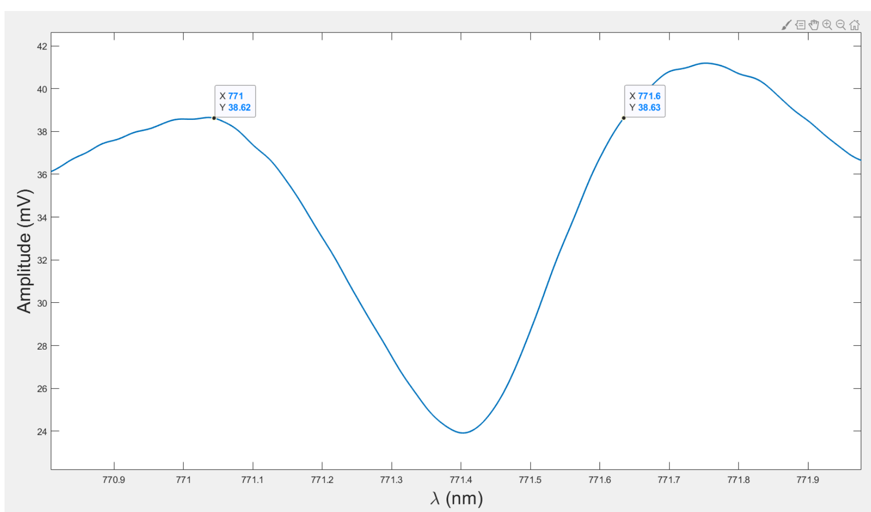

Figure B.1: Actual resonance plot of an optical resonator device

The parameters of the resonance curve in figure B.1 are

$$\lambda_r = 771.4\ nm, \lambda_{1,2} = 771\ nm, 771.6\ nm \tag{B.2}$$

From the parameters (B.1), the quality factor is found as

$$Q_{actual} = \frac{\lambda_r}{\lambda_2 - \lambda_1} = 351.35 \tag{B.3}$$

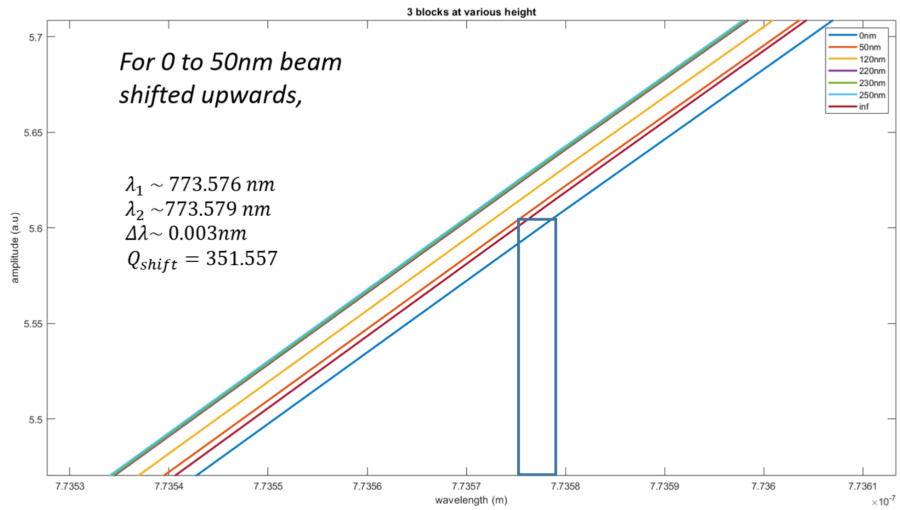

Figure B.2: Simulated resonance-shift plots

By assuming that the amount of change in the bandwidth in resonance shifting is negligible and that the ratio of shifted Q and the original Q stays the same, it gives

$$r = \frac{Q_{shift}}{Q} = \frac{\lambda_r - \Delta\lambda}{\lambda_r} \tag{B.4}$$

$$\frac{\lambda_{r,actual} - \Delta\lambda_{actual}}{\lambda_{r,actual}} = \frac{\lambda_{r,sim} - \Delta\lambda}{\lambda_{r,sim}} \tag{B.5}$$

The amount of shift in the wavelength in simulation due to 50 nm nanomechanical displacement of the structure is shown in figure B.2 to be 0.003 nm. Using this,

$$\frac{771.4 - \Delta\lambda}{771.4} = \frac{772.967}{772.96} \tag{B.6}$$

and the shift in the wavelength due to the modulation found from the simulation is

$$\Delta\lambda = 0.003nm \tag{B.7}$$

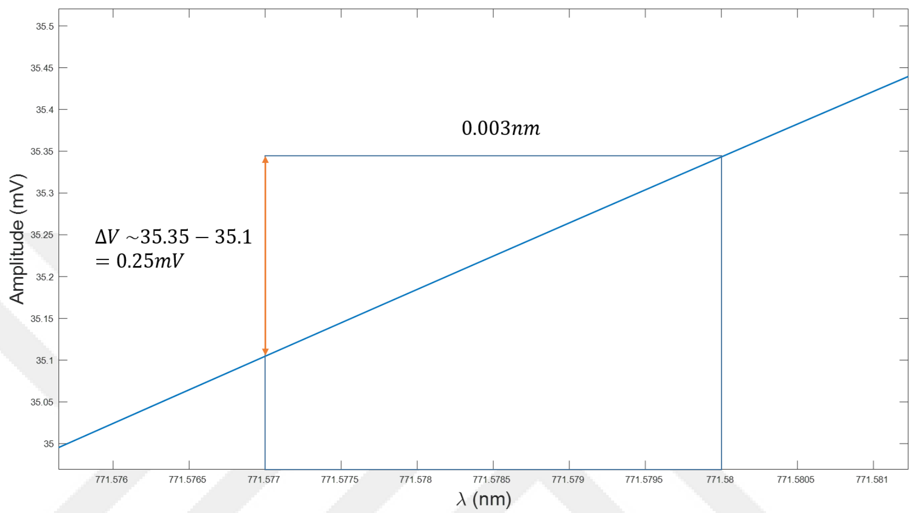

Figure B.3: Amount of voltage output shift on an actual resonance curve that corresponds to the wavelength shift found from the simulation. The resonance curve shown in Figure B.1 is used for the interpolation of the voltage shift.

Appendix C

Simulation of Three-beam Resonance Frequency

Here, a list of simulation results of three-beam nanomechanical structures' frequency modes is presented.

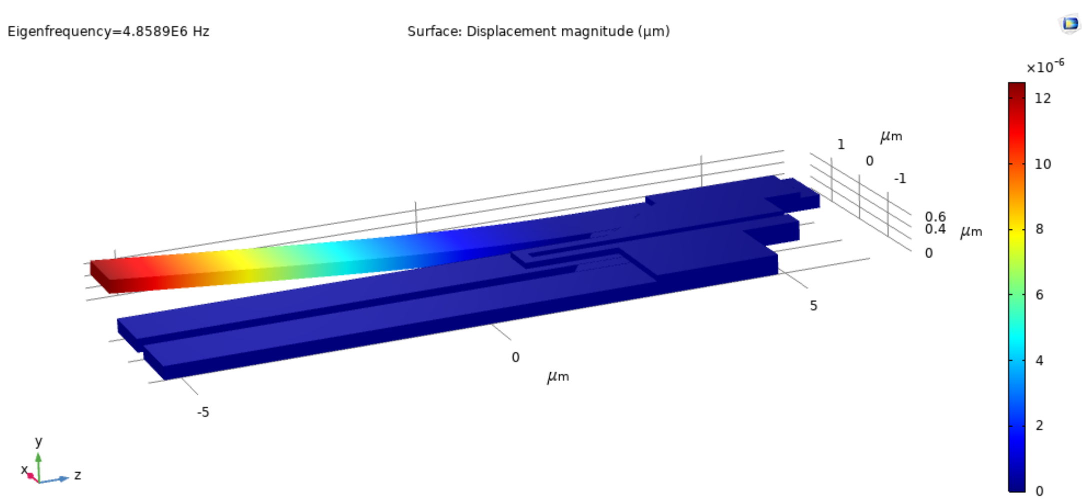

Figure C.1: 1st mode of the long beam

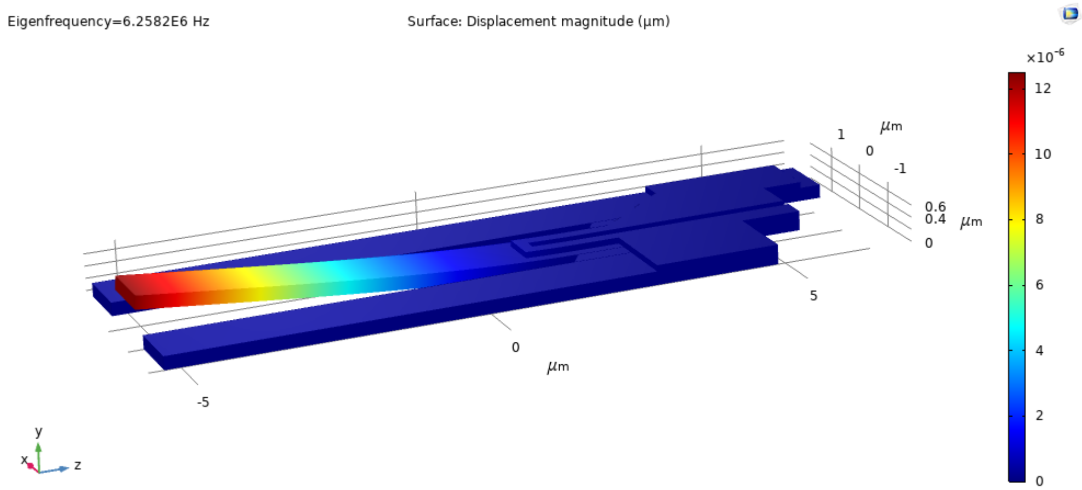

Figure C.2: 1st mode of the medium beam

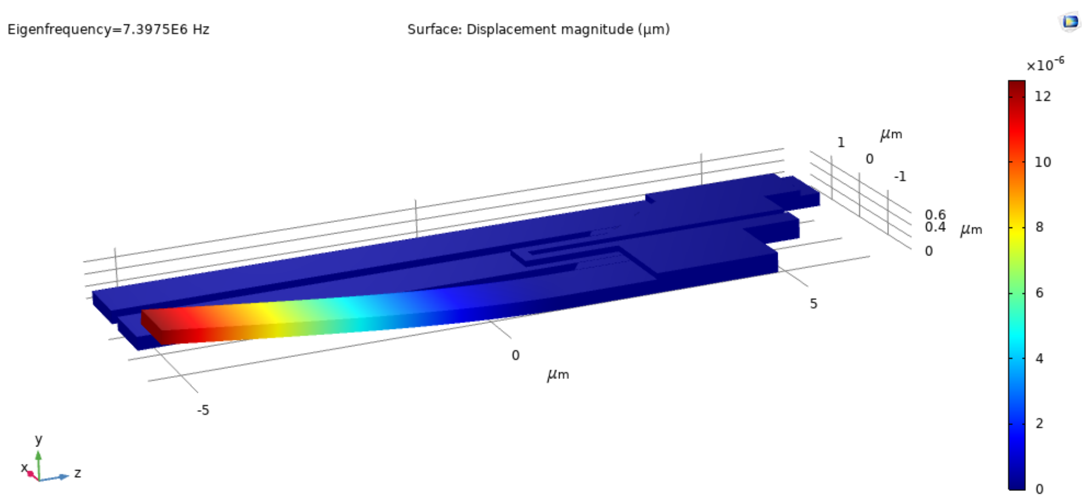

Figure C.3: 1st mode of the short beam

Appendix D

Microwave Cavity Mask Design

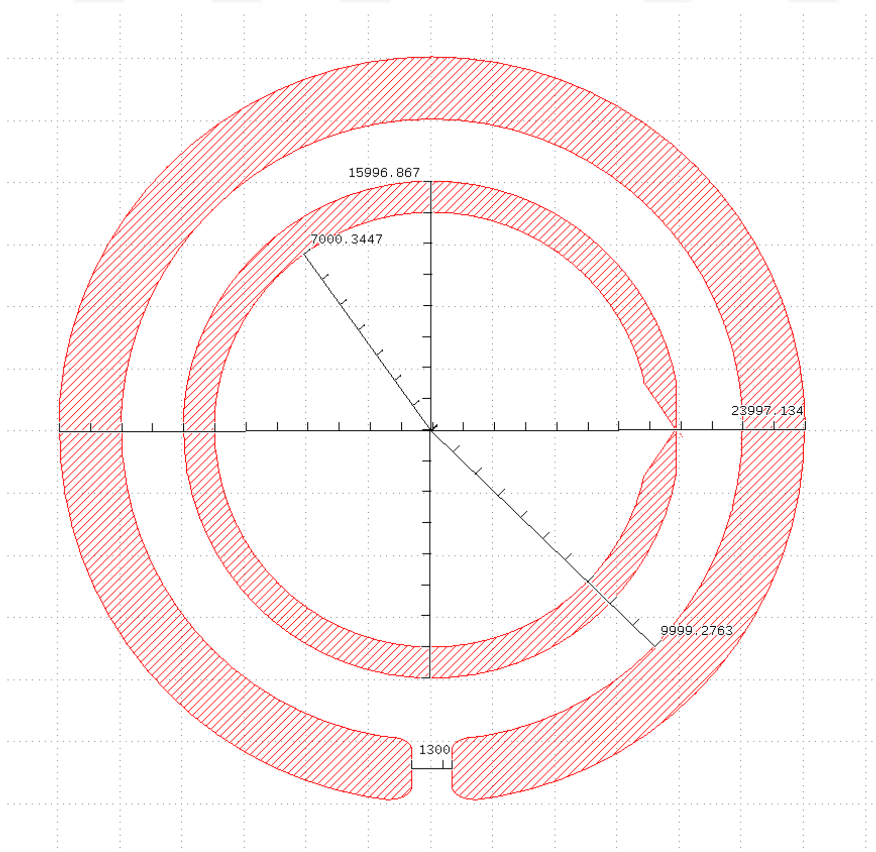

Figure D.1: CSRR design and dimensions